Earth and Planetary Science Letters 397 (2014) 184–200

Contents lists available at ScienceDirect

Earth and Planetary Science Letters

www.elsevier.com/locate/epsl

Thickening, refertilization, and the deep lithosphere filter in continental arcs: Constraints from major and trace elements and oxygen isotopes

Emily J. Chin [a,*], Cin-Ty A. Lee [a], Jaime D. Barnes [b]

[a] Dept. of Earth Science, Rice University, Houston, TX 77005, United States
[b] Dept. of Geological Sciences, Jackson School of Geosciences, University of Texas, Austin, TX 78712, United States

ARTICLE INFO

Article history:
Received 28 September 2013
Received in revised form 8 April 2014
Accepted 10 April 2014
Available online 14 May 2014
Editor: T.M. Harrison

Keywords:
Sierra Nevada
continental arc
peridotite
refertilization

ABSTRACT

Arc magmatism is a complex process involving generation of primary melts in the mantle wedge and chemical refinement of these melts into differentiated products akin to continental crust. Interaction of magmas (cooling, crystallization and assimilation) with the overlying crust, particularly if it is thick, is one way by which primary basalts are refined into more evolved compositions. Here, we explore the role of the mantle lithosphere as a trap and/or reactive filter of magmas. We use mantle xenoliths from the Sierra Nevada continental arc in California as a probe into sub-Moho processes. Based on clinopyroxene modal abundance and major, minor and moderately incompatible trace element concentrations, the peridotites define a refertilization trend that increases with depth, grading from clinopyroxene-poor (<5%), undeformed spinel peridotites equilibrated at <3 GPa (<90 km) to clinopyroxene-rich (10–20%), porphyroclastic garnet peridotites equilibrated between 3 and 3.5 GPa (90–105 km), the latter presumably approaching the top of the subducting slab. The petrology and geochemistry of the xenoliths suggest that the fertile peridotites were originally depleted spinel peridotites, which were subsequently refertilized. Incompatible trace element geochemistry reveals a pervasive cryptic metasomatic overprint in all peridotites, suggesting involvement of small amounts of subduction-derived fluids from the long-lived Farallon plate beneath western North America. However, bulk reconstructed $\delta^{18}O_{SMOW}$ values of the peridotites, including the most refertilized, fall between 5.4 and 5.9‰, within the natural variability of unmetasomatized mantle (~5.5 ± 0.2‰). Together with Sm, Yb, and Ca compositional data, the oxygen isotope data suggest that the role of slab or sediment melts in refertilizing the peridotites was negligible (<5% in terms of added melt mass). Instead, binary mixing models suggest that many of the Sierran garnet peridotites, particularly those with high clinopyroxene modes, had up to 30% mantle-derived melt added. Our data suggest that refertilization of the deep arc lithosphere, via melt entrapment and clinopyroxene precipitation, may be an important process that modifies the composition of primary arc magmas before they reach the crust and shallowly differentiate. Comparison of our data with a global compilation of arc-related mantle xenoliths suggests that sub-Moho refertilization may be more extensive beneath mature arcs, such as continental arcs, compared to juvenile island arcs, possibly because of the greater thickness of crust and lithosphere beneath mature and island arcs.

1. Introduction

Island arcs are potential building blocks of continents (Taylor, 1977), but an outstanding problem is how basalts, the dominant product of island arcs, are refined into andesitic continental crust. One end-member mechanism is single-stage differentiation of granitoids from a basaltic parent (Bowen, 1928; Gill, 1981; Grove and Baker, 1984; Lee et al., 2007b; Jagoutz et al., 2009). Another scenario is multi-stage differentiation of a basaltic parent involving re-melting and assimilation of pre-existing lower crust to generate granitoids (White and Chappell, 1977; Tatsumi et al., 2008). Primary magmas are mixed, assimilated, stored, and homogenized in deep crustal magma chambers (Hildreth and Moorbath, 1988; Annen et al., 2006), and upon ascent through shallower crust are further differentiated via lower pressure crystal fractionation and wallrock assimilation (DePaolo, 1981; Blatter et al., 2013; Bohrson and Spera, 2001; Lee et al., 2013; Dufek and Bachmann, 2010). Such deep crustal magma chambers may be favored

* Corresponding author. Tel.: +631 827 1198; fax: +713 348 5214.
E-mail address: ej3030@gmail.com (E.J. Chin).

http://dx.doi.org/10.1016/j.epsl.2014.04.022
0012-821X/

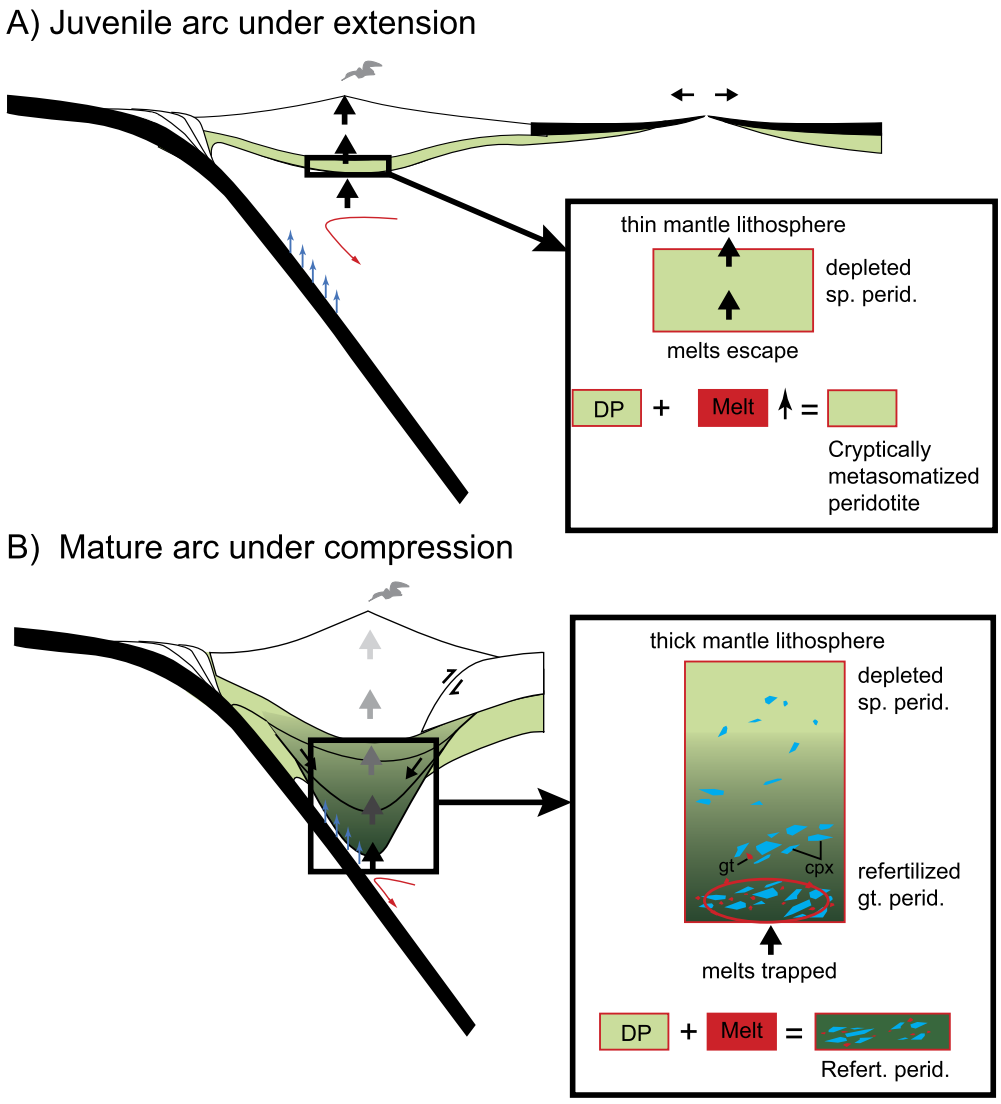

Fig. 1. Cartoon illustrating refertilization of the mantle lithosphere in juvenile and mature arcs. In A), mantle lithosphere is thin beneath juvenile arcs under extension. Primary magmas from the mantle wedge do not stagnate extensively beneath the lithosphere, bypassing it and erupting as basaltic magmas (black arrows). However, cryptic metasomatism of the mantle could occur, but this would not result in the formation of new mineral phases. In B), mantle lithosphere is thick beneath mature arcs under compression. Primary magmas from the mantle wedge might stagnate extensively beneath the lithosphere and undergo increased differentiation (black to gray arrows), and also experience high-pressure crystal fractionation which results in clinopyroxene-enrichment of the mantle. This type of modal metasomatism results in refertilization.

beneath thick, mature island and continental arcs, because primary magmas may be more easily trapped beneath thick crust, enhancing differentiation to more felsic compositions (Leeman, 1983). Indeed, crustal deformation studies of arc volcanoes suggest that deep crustal magma chambers are more prevalent beneath compressional, thick continental arcs compared to extensional, thin island arcs (Chaussard and Amelung, 2012). As a consequence, continental arc magmas may experience greater differentiation and processing through thicker crustal columns, erupting a larger proportion of andesites, compared to their island arc counterparts where the crust is thinner and the magma flux is dominated by basalt (Fig. 1).

Despite the focus on the crust and its effect on magmatic differentiation in arcs (Plank and Langmuir, 1988; Wallace and Carmichael, 1999), comparatively few studies have addressed the role of the mantle lithosphere. One important question in the study of arc magmatism (and magmatism in general) is how much differentiation of a primary melt occurs below the crust? This question is important because in some arcs, particularly mature continental arcs, such as the Andes in South America and Sierra Nevada in the Western USA, the deep sub-Moho arc lithosphere can reach considerable thickness (Kay et al., 1994; Ducea and Saleeby, 1996; Lee et al., 2001a; Haschke and Gunther, 2003; Chin et al., 2012). Field and xenolith studies from paleo-arcs such as the Sierra Nevada (Lee et al., 2006), Talkeetna (Greene et al., 2006), and Kohistan (Jagoutz et al., 2009, 2011) reveal an abundance of mafic cumulates at lower crustal depths. While these cumulates provide evidence for deep crustal crystal fractionation of primitive arc magmas, how much crystal fractionation occurs within the underlying mantle lithosphere is not well known. Because thicker crust favors fractionation of high-pressure phases (e.g., pyroxene over olivine; Chen and Presnall, 1975), it might be expected that thicker lithosphere would also promote the fractionation of such phases. As a consequence, “primary” arc magmas may undergo crystal fractionation at greater depths than previously recognized. Furthermore, melts passing through depleted arc mantle can react with and modally metasomatize (refertilize) the mantle, transforming it back into fertile lherzolite (Fig. 1B).

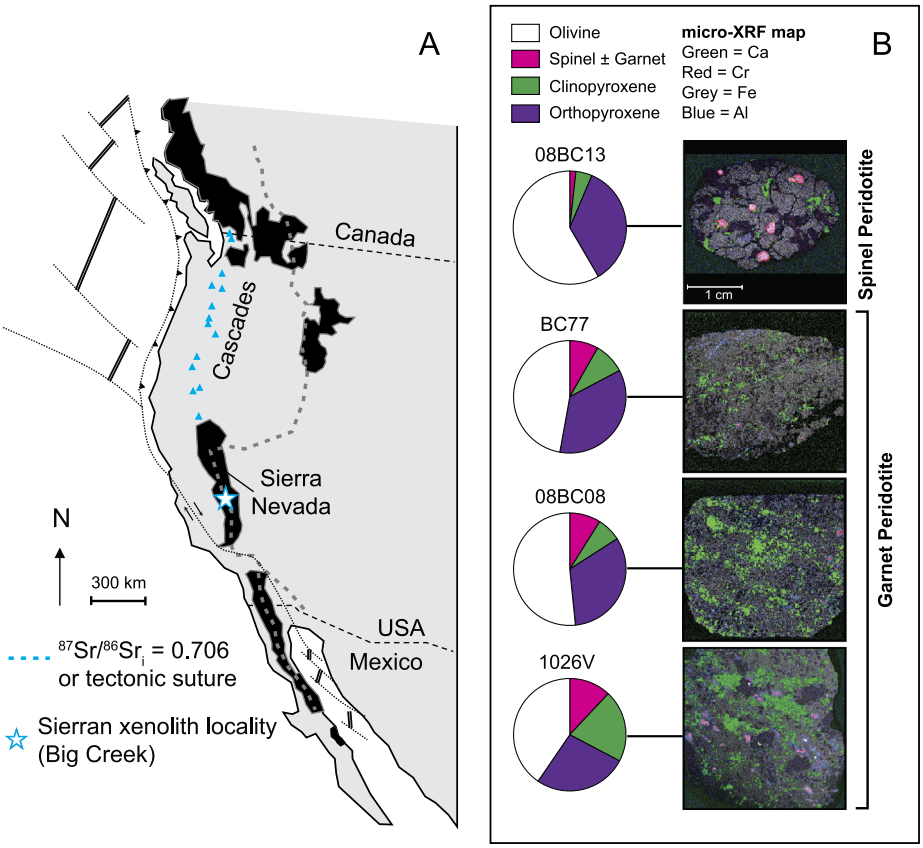

Fig. 2. A) Map of study area, with locality of Sierran peridotite xenoliths shown by star. B) Modal mineralogies and micro-XRF maps of representative Sierran peridotites. (For interpretation of the references to color in this figure, the reader is referred to the web version of this article.)

Evaluating the relative contributions of crustal versus mantle processes in arc magmatism is difficult because few arc magmas preserve memory of their inception and early evolution in the mantle. Mantle xenoliths, however, provide a potential window into sub-Moho processes beneath arcs. Previous studies of such xenoliths in various oceanic island arcs show evidence of interaction between depleted mantle and hydrous fluids and/or melts (Maury et al., 1992; Kepezhinskas et al., 1996; McInnes et al., 2001; Ionov, 2010). Mantle xenoliths from continental arcs are found in the Sierra Nevada in the Western USA (Dodge et al., 1988; Mukhopadhyay, 1989; Mukhopadhyay and Manton, 1994; Ducea and Saleeby, 1996; Lee et al., 2001a, 2001b; Chin et al., 2012, 2013), Mexico (Liang and Elthon, 1990; Luhr and Aranda-Gomez, 1997; Blatter and Carmichael, 1998); and the Canadian Cordillera (Peslier et al., 2002). Other studies from continental arcs examined peridotites from back-arc settings, such as the Simcoe volcanic field behind the Cascades arc (Brandon and Draper, 1996). Most, if not all, published arc xenolith studies involved only peridotites from the spinel facies. A notable exception is the Sierra Nevada xenoliths from California, many of which sample the garnet facies and thus offer a rare view of the deep lithosphere beneath a mature continental arc.

The goal of this paper is to place better constraints on what influence the deep lithosphere has on the compositional evolution of continental arcs. Owing to their generally thicker lithosphere, continental arcs could undergo more extensive sub-Moho magmatic differentiation compared to oceanic arc settings, which generally have thinner lithosphere (Gill, 1981). Does the deep arc lithosphere have an analogous role to thick crust, acting as a trap or reactive filter for ascending arc magmas? How does the deep arc lithosphere evolve compositionally, given that primary melts impinge and pass through it? What is the role of slab-derived melts and/or fluids in the compositional development of the deep lithosphere or as metasomatic agents in the mantle wedge (Straub et al., 2013)?

To address the questions above, we use a suite of peridotite xenoliths from the Sierra Nevada arc in California, USA. The Sierra Nevada is one of the type localities of a mature, continental arc, and among the best-studied arcs in the world. We synthesize textural, compositional, and oxygen isotope data on Sierran peridotites, and show that magma-wallrock interaction and crystal fractionation extends far below the Moho in some continental arcs.

2. Geologic setting

The Sierra Nevada Batholith was a long-lived (220–80 Ma) (Stern et al., 1981) continental arc that formed due to subduction of the Farallon Plate beneath western North America (Fig. 2A). The Mid to Late Cretaceous witnessed a period of especially voluminous magmatism, peaking at ~93 Ma (Chen and Moore, 1982; Barton, 1996; Coleman and Glazner, 1997). Magmatism was concomitant with compressional deformation at all levels of the lithosphere, ranging from upper crustal fold-and-thrust belts (Sevier Orogeny), continental underthrusting beneath the arc at middle to lower crustal levels (DeCelles et al., 2009; Chin et al., 2013), and thickening of the mantle lithosphere (Chin et al., 2012). By around 74 Ma, Sierran volcanism ceased and magmatism swept eastward into the continental interior (Coney and Reynolds, 1977). This shift is attributed to flattening of the Farallon slab (Laramide Orogeny) (Dickinson and Snyder, 1978; Bird, 1988; Saleeby, 2003), but magmatic thickening and pinch-out of the asthenospheric wedge may be another explanation (Chin et al., 2012). Following the Laramide Orogeny, roll-back of the slab induced ignimbrite flare-ups ~40 Ma

(Humphreys, 1995). At ~20 Ma, subduction of the Pacific-Farallon Ridge initiated the San Andreas Transform, the opening of a "slab-less window" (Atwater, 1970; Dickinson and Snyder, 1979), and the start of Basin and Range extension and basaltic volcanism which continues to present (Wernicke et al., 1988).

Low-volume but widespread ultrapotassic and alkalic basalts erupted synchronously with Basin and Range extension in the central and eastern Sierra Nevada (Moore and Dodge, 1980; Van Kooten, 1980). Geochemistry of the lavas reflect origin from a *K*-metasomatized mantle source enriched in Pb, Sr, and other fluid-mobile elements (Feldstein and Lange, 1999; Farmer et al., 2002), probably inherited from Mesozoic subduction of oceanic lithosphere beneath Western North America. The Cenozoic magmatic activity is divided into three episodes: Miocene (8–12 Ma), Pliocene (3–4 Ma), and Quaternary (0–1 Ma) (Ducea and Saleeby, 1996). By the early Miocene, the slab window had begun to open beneath the southern Sierra Nevada (Atwater and Stock, 1998). Upwelling of asthenosphere induced by the slab window and associated crustal extension may have facilitated melting of Sierran deep lithosphere and is thought to be a cause of late Miocene magmatism in the central and eastern Sierra Nevada (Farmer et al., 2002). Miocene lavas contain garnet-bearing deep lithospheric xenoliths, including garnet peridotites (Dodge et al., 1988; Mukhopadhyay and Manton, 1994; Ducea and Saleeby, 1996; Lee et al., 2001a), and thus attest to the presence of a thick (~100 km) mantle root that was present in Miocene times. In contrast, the lack of garnet-bearing xenoliths in Pliocene lavas suggests that the ~100 km lithospheric root was removed by the time of these eruptions 3–4 Ma ago (Lee et al., 2000).

Of particular interest to this study and numerous previous investigations (Dodge et al., 1988; Mukhopadhyay and Manton, 1994; Ducea and Saleeby, 1996; Lee et al., 2001a, 2001b) is the Late Miocene Big Creek diatreme (37°13′N, 119°16′W). Big Creek contains a wealth of xenoliths which have been used to reconstruct the stratigraphy of the deep arc lithosphere (Saleeby et al., 2003). Starting at the base of the seismically defined crust (Fliedner and Ruppert, 1996), the lithosphere grades from low-Mg pyroxenitic cumulates, to high-Mg pyroxenites interleaved with spinel peridotite, and finally into garnet-bearing spinel peridotite (hereafter referred to as "garnet peridotite") at the base of the lithosphere (Saleeby et al., 2003; Lee, 2014). According to Lee et al. (2006), low-Mg pyroxenites are thought to represent cumulates of evolved, hydrous basalt at lower crustal conditions (1.5 GPa). High-Mg pyroxenites are considered higher pressure (2–3 GPa) cumulates of a primary, hydrous basalt. The peridotites are thought to represent the deepest samples of the sub-arc lithosphere, with some garnet peridotites recording equilibration up to 3.6 GPa (Ducea and Saleeby, 1998; Chin et al., 2012). In this paper, we build on the work of Chin et al. (2012), who focused on the pressure–temperature-compositional history of Sierran garnet peridotites. Combined with previously published data from Dodge et al. (1988), Lee et al. (2001a), Lee (2005), and Chin et al. (2012), here we report new whole-rock and mineral compositional data on Sierran peridotite xenoliths.

3. Methods

Whole-rock major elements and selected trace elements were analyzed by XRF at Washington State University at Pullman. Additional details regarding the XRF method and analytical precision can be found online at http://environment.wsu.edu/facilities/geolab.

Trace element abundances were also determined by ICP-MS using a ThermoFinnigan ELEMENT 2 at Rice University. Whole rocks were crushed in a ceramic SPEX mill and powdered in a shatterbox. For trace element analysis, 50–80 mg of whole rock powder from each sample was added to a 2.5 ml Savillex wrench-top beaker. After two sequential open-beaker digestions using a 1:1 HF:$HClO_4$ mixture and complete open-air dry-down at ~190 °C, the samples were diluted to total volume ~125 ml in 2% HNO_3. 0.025 ml of concentrated HCl was added to each sample to keep Fe in solution. A 1 ppb In tracer was added to each sample as an internal standard. External standards (USGS powders BHVO-1, BIR-1, AGV-1, DTS-1, JP-1; values from Eggins et al., 1997) and procedural blanks were prepared along with all unknown samples and analyzed in the same runs. Li, Ga, Rb, Sr, Y, Zr, Nb, Cs, Ba, the rare earth elements (REE), Ta, Tl, Pb, Thu, and U were analyzed in low resolution ("low resolution ICP-MS or LR-ICPMS" where $m/\Delta m = 300$). Sc, V, Cr, Co, Ni, Cu, Zn were analyzed in medium resolution ("medium resolution ICP-MS or MR-ICPMS" where $m/\Delta m = 3000$). RSD (relative standard deviation) for all trace elements analyzed is <10%, with most elements ranging between 1 and 5%.

Major element compositions of minerals (olivine, orthopyroxene, clinopyroxene, spinel) in spinel peridotites 08BC10, BC10-1, BC10-2 and BC10-4 were acquired using wavelength-dispersive spectroscopy electron probe micro-analysis (EPMA) using a CAMECA SX50 at Texas A&M University. Mineral data is reported in the Supplemental Tables S1, S2, S3, and S4. Spot size was 1 micron, operating conditions were 15 kV accelerating voltage, 5 nA current, and 40 ms dwell time. Orthopyroxene, clinopyroxene, garnet, olivine, and chromite standards were used.

For oxygen isotope analysis, minerals were separated as follows. Whole rocks for 3 garnet peridotites (08BC03, 08BC08, 08BC04), 3 spinel peridotites (08BC13, BC10-1, 08BC10), and 4 garnet pyroxenites (BC98-7, BC98-5, BC98-9, BCX) were gently disaggregated using a rock hammer; the freshest, least altered gravel-sized pieces were then gently crushed in an agate mortar and sieved for grain sizes between 250 and 500 μm. From this size fraction, approximately 2 mg of minerals (olivine, orthopyroxene, clinopyroxene; garnet was picked from 1 garnet peridotite as well as from the garnet pyroxenites) from each sample were hand-picked under a binocular microscope. Only the cleanest, "gem"-like, alteration- and inclusion-free grains were selected. The mineral separates were then cleaned for several hours in dilute HCl, ultrasonicated, and rinsed in de-ionized water.

Oxygen isotope ratios were determined using the laser fluorination technique of Sharp (1990) at the University of Texas at Austin. ~2 mg of sample was heated with a CO_2 laser in the presence of BrF_5 and subsequently cryogenically purified using the silicate extraction line before introduction into a ThermoElectron MAT 253 isotope ratio mass spectrometer. In order to check for precision and accuracy of oxygen isotope analyses, garnet standard UWG-2 ($\delta^{18}O = +5.8‰$) (Valley et al., 1995), in-house olivine standard San Carlos ($\delta^{18}O = +5.2‰$), and in-house quartz standards Gee Whiz ($\delta^{18}O = +12.6‰$) and Lausanne-1 ($\delta^{18}O = +18.1‰$) were run. All $\delta^{18}O$ values are reported relative to SMOW, where the $\delta^{18}O$ value of NBS-28 is +9.65‰. Precision based on replicates of standards is ±0.09‰.

4. The Sierran peridotite xenoliths

4.1. Sample descriptions

The Sierran peridotite suite is comprised of 14 spinel peridotites and 13 garnet peridotites (Table 1). Here, we report new whole-rock major element and trace element data on 8 spinel peridotites (08BC01, 08BC10, BC10-1, BC10-2, BC10-3, BC10-4, BCPL10-5, BC10-6) and 4 garnet peridotites (08BC05, 08BC11, 08BC23, P6). Only those samples with >95% anhydrous major element oxide totals are of interest here. Furthermore, new mineral data are reported (Supplemental Tables S1–S4) for 08BC10, BC10-1, BC10-2, and BC10-4. Of the new samples analyzed, 3 of

Table 1
Whole-rock geochemistry and $\delta^{18}O$ values of mineral separates.

		Spinel peridotites													
	Reference	08BC01[a] This study	08BC02 3	08BC06 3	08BC10 This study	08BC13 3	P-7 2	P-10 2	BC98-2 2	BC10-1 This study	BC10-2 This study	BC10-3 This study	BC10-4 This study	BCPL10-5 This study	BC10-6 This study
XRF	Weight percent		Moderate serp.									Moderate serp.			
XRF	SiO_2	47.70	44.85	47.90	45.10	45.52	45.45	48.97	46.18	45.64	47.05	53.50	44.95	44.89	48.09
XRF	TiO_2	0.03	0.04	0.03	0.02	0.01	0.09	0.05	0.03	0.01	0.03	0.01	0.02	0.06	0.05
XRF	Al_2O_3	0.71	2.10	1.63	1.29	1.49	3.42	1.99	3.18	1.69	1.52	0.93	1.18	2.22	2.09
XRF	Cr_2O_3	0.18	0.34	0.40	0.33	0.43				0.39	0.41	0.44	0.37	0.41	0.36
XRF	FeOT	6.65	8.32	7.75	8.49	7.79	8.23	8.01	7.65	7.94	8.03	6.91	7.66	8.99	7.35
XRF	MnO	0.11	0.14	0.26	0.13	0.13	0.14	0.21	0.14	0.14	0.12	0.28	0.12	0.15	0.23
XRF	MgO	44.03	42.31	38.45	43.26	43.32	39.24	38.16	40.01	42.74	41.23	34.10	44.55	39.92	37.38
XRF	CaO	0.54	1.48	3.47	1.31	1.24	3.14	2.36	2.49	1.41	1.45	3.79	1.11	3.17	4.20
XRF	Na_2O	0.06	0.20	0.08	0.03	0.04	0.28	0.17	0.21	0.03	0.07	0.00	0.01	0.13	0.11
XRF	K_2O	0	0.14	0.03	0.01	0.01	0.01	0.05	0.09	0.01	0.07	0.03	0.01	0.04	0.13
XRF	P_2O_5	0	0.07	0.02	0.02	0.01	0.01	0.01	0.02	0.01	0.02	0.01	0.01	0.02	0.02
	Total	100	100	100	100	100	100	100	100	100	100	100	100	100	100
	Difference		1.82	4.15	3.14	2.01	1.02	1.19	0.62	2.53	3.58	4.00	1.60	1.29	5.84
	Mg#	92.19	90.06	89.85	90.08	90.84	89.47	89.46	90.31	90.57	90.15	89.80	91.21	88.79	90.07
	ppm														
LR-ICPMS	Li	5.05	17.7	14.4	20.3	5.41	3.47	19.1	7.23	22.7	27.0	43.4	31.8	10.8	39.5
MR-ICPMS	Sc	6.24	5.91	8.18	7.93	9.49	12.9	6.75	10.7	8.95	6.55	9.52	8.67	12.3	10.7
XRF			8	9	8	10				8	8	8	8	12	11
MR-ICPMS	V	20.9	26.8	41.0	33.8	41.0	59.2	36.6	43.0	38.2	27.8	39.6	37.1	60.3	48.2
XRF			36	42	35	45				44	39	28	36	63	52
MR-ICPMS	Cr														
XRF			2358	2751	2265	2954				2688	2827	3044	2555	2794	2459
MR-ICPMS	Co	107	121	96	108	103	112	116	109	97	123	100	104	113	124
MR-ICPMS	Ni	2295	2268	2050	2223	2068	2415	2490	2504	2120	2778	2526	2412	2272	2261
XRF			2405	2072	2419	2210				2272	2420	2079	2441	2114	2130
MR-ICPMS	Cu	7.28	27.6	18.9	6.88	6.39	24.8	1.95	1.26	8.36	15.6	17.7	15.7	27.0	7.76
XRF			14	24	11	12				7	6	8	12	30	11
MR-ICPMS	Zn	38.7	40.3	41.9	47.7	42.3	44.4	51.2	48.6	38.3	38.0	42.4	45.1	43.4	31.6
XRF			46	48	51	49				49	50	44	44	56	44
LR-ICPMS	Ga	0.65	1.24	1.42	1.22	0.96	2.95	1.94	2.59	1.32	1.35	2.71	1.13	2.43	1.92
XRF			3	3	3	2				2	1	2	0	3	1
LR-ICPMS	Rb	1.09	7.75	2.62	2.26	1.00	1.20	5.89	5.05	0.75	9.47	10.51	0.57	2.47	9.83
XRF			9	2	2	0				0	11	7	0	2	10
LR-ICPMS	Sr	6.90	31.0	41.0	25.5	17.0	20.7	58.9	61.3	11.2	37.7	102	8.10	61	93
XRF			52	41	26	17	N/A	N/A	N/A	11	39	110	6	65	94
LR-ICPMS	Y	0.58	0.67		1.49	0.19	2.34	0.68	1.18	0.50	0.31	2.36	0.50	1.33	1.41
XRF			3	2	3	1				3	3	3	2	4	3
LR-ICPMS	Zr	1.72	8.52	1.12	0.52	0.51	4.40	1.75	5.90	1.29	2.76	1.34	2.30	3.56	3.64
XRF			13	3	2	2				1	5	2	3	5	4
LR-ICPMS	Nb	0.112	1.108	0.222	0.339	0.125	0.061	0.060	0.364	0.308	0.377	0.771	0.107	0.943	0.765
LR-ICPMS	Cs	0.60	2.99	2.54	1.74	0.85	1.09	5.13	2.73	0.65	9.99	9.69	0.64	1.37	9.18
LR-ICPMS	Ba	21.2	27.9	19.7	15.7	16.6	9.2	18.6	44.5	6.2	15.9	100	14.5	23.6	33.9
XRF			51	30	20	21				15	23	43	18	33	38
LR-ICPMS	La	0.189	2.01	0.992	0.778	0.0819	0.201	0.384	1.14	0.456	0.539	2.95	0.137	0.673	1.40
LR-ICPMS	Ce	0.337	3.59	0.846	0.353	0.142	0.559	0.411	2.15	0.653	1.02	2.57	0.239	1.23	1.78
LR-ICPMS	Pr	0.0468	0.389	0.0854	0.190	0.0186	0.105	0.0556	0.295	0.0839	0.137	0.269	0.0592	0.167	0.218
LR-ICPMS	Nd	0.210	1.42	0.349	0.799	0.079	0.589	0.254	1.21	0.306	0.555	1.02	0.388	0.721	0.905
LR-ICPMS	Sm	0.0609	0.234	0.0744	0.201	0.0212	0.211	0.0700	0.234	0.0579	0.113	0.184	0.115	0.202	0.208
LR-ICPMS	Eu	0.0238	0.0894	0.0271	0.0539	0.008	0.0855	0.0318	0.0784	0.0139	0.0350	0.0836	0.0333	0.0744	0.0706
LR-ICPMS	Gd	0.0735		0.107	0.244	0.0277	0.284	0.0883	0.216	0.0918	0.121	0.260	0.0891	0.205	0.237
LR-ICPMS	Tb	0.0147	0.0433	0.0147	0.0370	0.00433	0.0531	0.0151	0.0324	0.0099	0.0136	0.0259	0.0151	0.0357	0.0317
LR-ICPMS	Dy	0.0979	0.116	0.0920	0.229	0.0275	0.367	0.0918	0.188	0.0611	0.0732	0.142	0.0869	0.235	0.193
LR-ICPMS	Ho	0.0224	0.0227	0.0217	0.0494	0.0070	0.0887	0.0211	0.0425	0.0141	0.0114	0.0303	0.0181	0.0522	0.0402
LR-ICPMS	Er	0.0688		0.0685	0.152	0.0253	0.275	0.0631	0.139	0.0498	0.0335	0.0898	0.0573	0.157	0.122
LR-ICPMS	Tm	0.0112	0.0105	0.0105	0.0253	0.00542	0.0419	0.00984	0.0231	0.00876	0.00262	0.00936	0.00947	0.0211	0.0152
LR-ICPMS	Yb	0.0663	0.0698	0.0604	0.155	0.0321	0.260	0.0679	0.159	0.0554	0.0367	0.0686	0.0572	0.146	0.118
LR-ICPMS	Lu	0.0122	0.0109	0.0111	0.0257	0.0073	0.0401	0.0109	0.0262	0.0114	0.00667	0.0125	0.0111	0.0236	0.0194
LR-ICPMS	Hf	0.0575	0.188	0.0307	0.0148	0.0126	0.127	0.0501	0.156	0.0302	0.0805	0.0400	0.0575	0.112	0.106
LR-ICPMS	ID														
LR-ICPMS	Ta	0.0094	0.0691	0.013	0.032	0.0029	0.0045	0.0021	0.022	0.027	0.035	0.048	0.0065	0.056	0.092
LR-ICPMS	Tl	0.0480	0.0510	0.0170	0.0570	0.0210	0.0794	0.0595	0.0857	0.008			0.0190	0.0190	0.0210
LR-ICPMS	Pb	0.341	1.95	0.948	0.673	0.425	0.227	0.507	0.794	0.896	0.338	1.07	0.314	0.648	1.69
LR-ICPMS	Th	0.069	1.07	0.087	0.092	0.035	0.034	0.041	0.412	0.147	0.217	0.188	0.021	0.367	0.336
LR-ICPMS	U	0.0599	0.469	0.091	0.077	0.024	0.017	0.063	0.211	0.140	0.093	0.188	0.011	0.218	0.479

Table 1 (*continued*)

		Spinel peridotites													
		08BC01[a]	08BC02	08BC06	08BC10	08BC13	P-7	P-10	BC98-2	BC10-1	BC10-2	BC10-3	BC10-4	BCPL10-5	BC10-6
$\delta^{18}O_{SMOW}$ (‰) of mineral separates in selected samples															
	olivine				5.1	5.2				5.2					
	orthopyroxene				6.6	5.9				5.8					
	clinopyroxene				5.6	5.2				5.5					
	garnet														
	$\Delta_{cpx-olv}$				0.5	0.0				0.3					
	$\Delta_{opx-cpx}$				1.1	0.7				0.3					
	T (°C)opx-olv				685	1225				1215					
	T (°C)cpx-olv				1100					1450					

		Garnet-bearing spinel peridotites													Garnet pyroxenites			
	Reference	BC77 2	1026V 2	P-1 1	P-6 XRF from 3; ICPMS this study	96D-18 3	08BC03 3	08BC04 3	08BC08 3	08BC07 3	08BC05[b] This study	08BC14[b] 3	08BC11[b] This study	08BC23[b] This study	BC98-7 4	BC98-5 4	BC98-9 4	BCX 4
XRF	Weight percent										Serpentinized	Serpentinized	Serpentinized	Serpentinized				
XRF	SiO_2	47.55	47.95	45.30	45.73	48.46	46.65	50.75	46.67	46.89		49.76	51.73	46.36	50.1	50.25	43.57	45.65
XRF	TiO_2	0.03	0.03	0.12	0.14	0.15	0.06	0.19	0.02	0.03		0.07	0.07	0.06	0.37	0.62	0.43	0.41
XRF	Al_2O_3	2.60	3.59	2.78	4.20	6.63	3.16	4.81	2.43	1.86		3.28	4.06	2.39	8.62	7.59	10.01	15.27
XRF	Cr_2O_3				0.25		0.41	0.40	0.42	0.38		0.51	0.52	0.38			0	0
XRF	FeOT	7.54	7.08	8.93	8.24	7.61	7.68	8.06	7.74	7.66		7.71	6.45	7.37	11.43	9.61	13.45	13.69
XRF	MnO	0.14	0.15	0.15	0.13	0.15	0.25	0.12	0.13	0.16		0.61	0.82	0.45	0.22	0.19	0.53	0.30
XRF	MgO	39.17	35.48	37.62	37.31	33.14	37.00	31.07	40.26	41.87		25.83	24.82	32.49	20.26	17.88	4.42	9.91
XRF	CaO	2.76	5.40	4.81	3.61	3.45	4.56	3.98	2.17	1.08		11.89	11.31	10.29	8.18	13.08	26.62	12.83
XRF	Na_2O	0.19	0.28	0.29	0.34	0.35	0.13	0.48	0.11	0.03		0.18	0.14	0.12	0.70	0.71	0.70	1.40
XRF	K_2O	0.02	0.04	0.01	0.03	0.05	0.06	0.11	0.04	0.03		0.13	0.06	0.06	0.10	0.06	0.03	0.41
XRF	P_2O_5	0.00	0.00	0.00	0.01	0.01	0.03	0.03	0.01	0.02		0.03	0.02	0.02	0.01	0.01	0.23	0.11
	Total	100	100	100	100	100	100	100	100	100		100	100	100	100	100	100	100
	Difference	1.00	1.44	0.84	0.60	0.79	4.21	3.72	1.90	2.79		13.98	10.66	10.03	1.10	1.81	2.00	1.05
	Mg#	90.26	89.93	88.25	88.98	88.59	89.57	87.29	90.27	90.70		85.66	87.27	88.71				
	ppm																	
LR-ICPMS	Li	23.9	14.0		23.6		18.8	37.0	10.3	12.7	22.0	59.5	21.3	64.4	9.8	11	8.8	20
MR-ICPMS	Sc	8.98	17.6		12.1		15.9	16.6	12.1	5.85	7.64	12.8	14.4	8.58	48.6	62.7	8.1	52.8
XRF							14	17	13	9		14	19	12	53	59	0	53
MR-ICPMS	V	62.5	86.6		65.0		66.7	84.6	52.4	28.1	65.6	74.9	76.6	67.5	233	294	118	542
XRF							67	92	58	33		79	75	79	214	283	128	507
MR-ICPMS	Cr														2301	1731	112	105
XRF							2788	2770	2879	2621		3506	3588	2641	1829	1485	117	108
MR-ICPMS	Co	111	100		102		119	113	112	109	77.9	135	100	117	70.5	54.9	20.0	41.1
MR-ICPMS	Ni	2406	2297		1831		2505	2360	2380	2308	1284	2699	1515	2033	298.8	268.6	86.8	61.4
XRF							2124	1976	2182	2348		2249	1524	2213	283	233	52	51
MR-ICPMS	Cu	1.1	43.8		22.3		24.3	26.6	23.1	2.38	16.9	37.1	28.3	16.7	73.8	61.4	7.73	76.4
XRF							28	30	26	7		44	32	26	76	65	11	88
MR-ICPMS	Zn	49.6	50.2		42.9		29.1	33.2	29.2	38.0	37.8	30.6	49.9	37.3	90.2	68.1	54.0	155.2
XRF							42	57	45	48		58	52	45	82	69	55	155
LR-ICPMS	Ga	2.02	2.28				2.12	3.61	1.80	0.98	2.52	2.63	3.57	1.59	8.90	9.71	11.5	14.0
XRF							5	5	4	2		2	3	3	10	14	16	18
LR-ICPMS	Rb	2.02	2.58		3.65		4.97	13.1	2.18	2.50	5.00	14.2	5.33	6.67	2.4	1.03	0.857	11.4
XRF							5	13	2	2		13	6	8	3	2	0	13
LR-ICPMS	Sr	16.5	33.2		16.5		60.8	45.4	15.4	23.7	362	335	138	100	87.5	60.6	72.4	136.4
XRF							67	51	19	30		324	372	122	93	67	81	147
LR-ICPMS	Y	0.57	2.17				3.77	3.51	0.90	0.92	4.13	4.30	7.03	2.84	8.55	12.8	21.4	34.7
XRF							5	5	2	2		4	9	5	8	13	23	32

(*continued on next page*)

Table 1 (*continued*)

		Garnet-bearing spinel peridotites													Garnet pyroxenites			
	Reference	BC77 2	1026V 2	P-1 1	P-6 XRF from 3; ICPMS this study	96D-18 3	08BC03 3	08BC04 3	08BC08 3	08BC07 3	08BC05[b] This study	08BC14[b] 3	08BC11[b] This study	08BC23[b] This study	BC98-7 4	BC98-5 4	BC98-9 4	BCX 4
LR-ICPMS	Zr	4.39	4.46		5.08		3.61	9.54	0.63	0.98	1.73	3.44	5.15	2.28	11.2	21.3	56.6	25.3
XRF							10	12	2	2		5	4	3	15	26	67	34
ID															8.92	18.4	56.3	22.3
LR-ICPMS	Nb	0.043	0.066		0.154		0.184	0.153	0.051	0.197	0.140	0.209	0.139	0.299	0.304	0.224	0.157	1.45
LR-ICPMS	Cs	1.67	2.85		4.96		3.76	6.28	1.78	1.71	3.94	12.6	4.49	6.55	0.117	0.205	0.288	1.86
LR-ICPMS	Ba	16.9	9.80		17.8		57.5	50	20.4	25.9	73	112	42	67	257	50	14	184
XRF							64	53	29	44		111	98	79	245	61	13	186
LR-ICPMS	La	0.245	0.228		0.923		0.863	0.758	0.115	0.267	2.79	2.41	2.97	1.12	0.990	0.971	8.27	2.63
LR-ICPMS	Ce	0.850	0.877		0.803		1.26	1.58	0.231	0.407	2.88	2.53	3.05	1.55	3.01	3.68	17.9	6.28
LR-ICPMS	Pr	0.0760	0.0680		0.258		0.166	0.258	0.0300	0.0614	0.299	0.294	0.350	0.185	0.494	0.700	2.80	0.888
LR-ICPMS	Nd	0.317	0.315		1.33		0.740	1.37	0.137	0.305	1.22	1.27	1.65	0.792	2.74	4.24	13.4	5.03
LR-ICPMS	Sm	0.0599	0.100		0.398		0.203	0.439	0.0471	0.0929	0.246	0.296	0.448	0.190	0.901	1.58	3.02	2.90
LR-ICPMS	Eu	0.0233	0.0417		0.138					0.0566	0.154		0.208	0.124	0.708	0.573	1.42	1.28
LR-ICPMS	Gd	0.0741	0.160				0.282	0.499	0.0651			0.425			0.799	1.37	3.39	2.18
LR-ICPMS	Tb	0.0121	0.0323		0.0695		0.0580	0.0924	0.0154	0.0153	0.0515	0.0655	0.0855	0.0380	0.142	0.244	0.541	0.424
LR-ICPMS	Dy	0.103	0.295		0.575		0.452	0.589	0.121	0.130	0.307	0.434	0.763	0.327	1.01	1.66	3.14	3.35
LR-ICPMS	Ho	0.0172	0.0767		0.127		0.122	0.131	0.0321	0.0300	0.0716	0.106	0.176	0.0817	0.298	0.461	0.639	1.17
LR-ICPMS	Er	0.0465	0.259				0.414	0.379	0.109		0.184	0.337	0.397	0.203	0.853	1.29	1.90	3.46
LR-ICPMS	Tm	0.0070	0.0422		0.0547		0.0671	0.0561	0.0185	0.0147	0.0263	0.0505	0.0757	0.0442	0.125	0.188	0.283	0.516
LR-ICPMS	Yb	0.0420	0.273		0.300		0.440	0.355	0.123	0.0849	0.139	0.319	0.403	0.249	0.730	1.11	1.68	2.99
LR-ICPMS	Lu	0.0063	0.0427		0.0463		0.0696	0.0533	0.0203	0.0139	0.0209	0.0521	0.0621	0.0420	0.112	0.162	0.246	0.452
LR-ICPMS	Hf	0.110	0.104		0.188		0.111	0.283	0.0196	0.0303	0.0667	0.116	0.186	0.0814	0.432	0.845	1.90	0.884
ID															0.386	0.862	2.10	0.903
LR-ICPMS	Ta	0.0023	0.0038		0.0149		0.0093	0.0117	0.0031	0.0187	0.00839	0.0112	0.0100	0.0179	0.023	0.025	0.029	0.088
LR-ICPMS	Tl	0.0624	0.129				0.193	0.351	0.129	0.026	0.05	0.291	0.05	0.08	0.082	0.235	0.012	0.151
LR-ICPMS	Pb	0.236	0.603		0.464		0.214	1.12	0.155	0.184	1.37	0.664	1.36	0.366	0.413	0.551	0.223	1.53
LR-ICPMS	Th	0.0077	0.0087		0.078		0.181	0.175	0.0126	0.058	0.058	0.157	0.037	0.116	0.019	0.060	1.202	0.495
LR-ICPMS	U	0.011	0.007		0.116		1.02	0.0821	0.0158	0.185	0.094	2.98	0.368	5.65	0.142	0.030	0.779	0.242
$\delta^{18}O_{SMOW}$ (‰) of mineral separates in selected samples																		
	olivine						5.2	5.4	5.4									
	orthopyroxene						6.2	6.0	5.8									
							6.0	6.0										
	clinopyroxene						5.5	5.7	5.9									
							5.4											
	garnet						5.3								6.7	5.5	6.5	10.6
																		10.8
	$\Delta_{cpx-olv}$						0.3	0.2	0.5									
	$\Delta_{opx-cpx}$						0.6	0.3	-0.1									
	T (°C)opx-olv						1000	1330	1585									
	T (°C)cpx-olv						1630	1690	1130									

Difference = Normalized XRF total (100% volatile-free basis) – Unnormalized XRF total
Mg# = (atomic Mg/(Mg + FeT) × 100)
LR-ICPMS = low resolution ICPMS ($m/\Delta m = 300$)
MR-ICPMS = medium resolution ICPMS ($m/\Delta m = 3000$)
[1] Dodge et al., 1988
[2] Lee, 2005
[3] Chin et al., 2012
[4] Lee et al., 2006
[a] Major elements recalculated from solution MR-ICPMS (SiO_2 determined by difference). Sample is fresh and un-serpentinized in hand specimen.
[b] Highly serpentinized samples (not plotted in Figs. 2, 3, 6, 7)

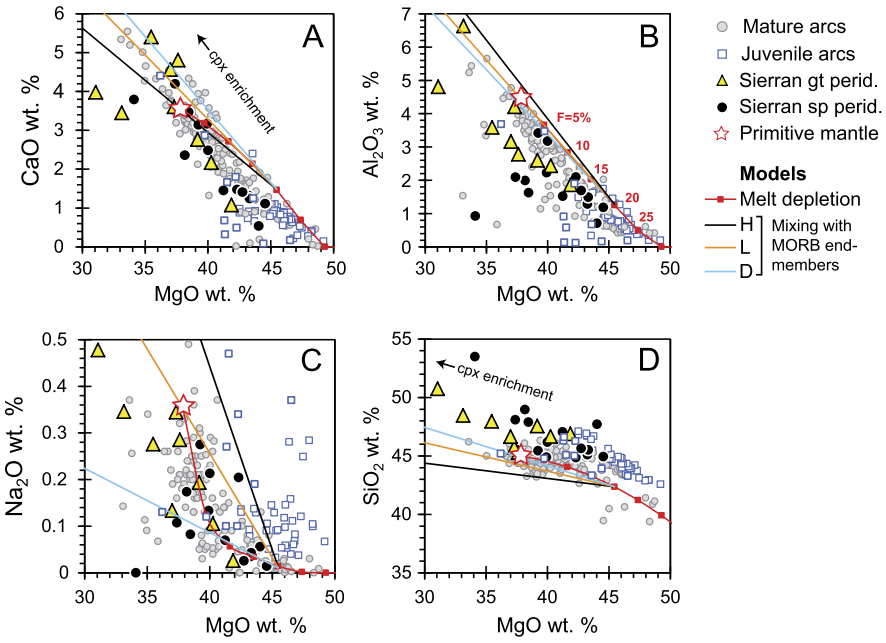

Fig. 3. CaO (A), Al_2O_3 (B), Na_2O (C) and SiO_2 (D) plotted against MgO (wt.%). Sierran spinel peridotites are shown as black circles and Sierran garnet peridotites as yellow triangles. Gray circles represent literature-compiled arc peridotites from mature island and continental arcs (Mexico, Canadian Cordillera, Kamchatka, Lesser Antilles, Philippines, and Ichinomegata) (see text for references). Blue squares represent global arc peridotites from juvenile island arcs and backarcs (Izu Bonin, South Sandwich, and Simcoe) (see text for references). Primitive mantle of McDonough and Sun (1995) shown as star. Melt depletion curves of primitive mantle are shown as red lines (see text for details). Black, orange, and blue lines represent mixing between 20% depleted primitive mantle and MORB end-members H, L, and D from Elthon (1992) (see text for details). (For interpretation of the references to color in this figure legend, the reader is referred to the web version of this article.)

the 4 garnet peridotites (08BC05, 08BC11, 08BC23) are extensively serpentinized with anhydrous whole-rock totals <90%. In addition, these 3 samples show evidence of carbonate infiltration, borne out in their high CaO (>10 wt.%) and high Sr (>100 ppm). We thus exclude these 3 samples from further discussion owing to the uncertainty in how serpentinization and other alteration processes have affected whole-rock compositions, but report all data in Table 1 for completeness.

4.2. Xenolith textures

Previous studies of Sierran mantle xenoliths (Ducea and Saleeby, 1996; Lee et al., 2001a; Chin et al., 2012) showed that the subarc mantle is compositionally stratified. The lithosphere transitions from shallow spinel peridotites (<3 GPa) into deep (3–3.5 GPa) garnet peridotites. The lithological transition is not sharp, as shown by the overlap in modal clinopyroxene between spinel and garnet peridotites (modal mineralogies are reported in Supplemental Table S5). Despite the overlap, spinel and garnet peridotites exhibit disparities in mineral modes and petrographic textures. In general, spinel peridotites have <10% clinopyroxene and have a coarse-grained, protogranular texture. Garnet peridotites have higher clinopyroxene modes (up to 20%) and are characterized by a fine-grained, highly deformed and recrystallized porphyroclastic texture (Chin et al., 2012; Fig. 2B).

Another distinction between spinel and garnet peridotites, as discussed in Chin et al. (2012), is that in garnet peridotites, clinopyroxene occurs in fine-grained, diffuse bands juxtaposed on the relict olivine-dominated matrix. These clinopyroxene bands were interpreted as evidence for melt infiltration, and combined with geochemical data, were used to suggest that the garnet peridotites experienced refertilization by basaltic melt. In this paper, we aim to place better constraints on the nature and magnitude of the refertilization.

5. Results

5.1. Whole-rock geochemistry

5.1.1. Major element composition

Major element data are reported in Table 1 and selected oxides (wt.%) are plotted against MgO (wt.%) in Fig. 3. Negative trends are observed in the Sierran data between CaO, Al_2O_3, Na_2O, and SiO_2 versus MgO. Garnet peridotites generally plot at the low-MgO, "fertile" end whereas spinel peridotites trend towards the high-MgO, "depleted" end. However, no sharp boundary separates the two peridotite groups in any of the binary oxide plots, with some spinel peridotites overlapping in composition with garnet peridotites. Several garnet peridotites are enriched in CaO, even more so than primitive mantle (McDonough and Sun, 1995) (Fig. 3A). These garnet peridotites also have high modal abundances of clinopyroxene (Fig. 2).

5.1.2. Trace elements

Trace element abundances are reported in Table 1. Spinel peridotites are distinguished from garnet peridotites by having mostly flat rare earth element (REE) element primitive mantle normalized patterns (not shown). In contrast, several garnet peridotites have normalized REE patterns that are enriched in the heavy REEs (HREE) relative to the middle REEs (MREE) (Chin et al., 2012). If all trace elements are plotted in order of increasing compatibility with respect to anhydrous melting of peridotite (Hofmann, 1988), both spinel and garnet peridotites show depletion in Nb relative to La, as well as depletion in Ti relative to Sm (Fig. 4). Positive anomalies in fluid-mobile elements (Cs, Li, Ba, Rb, Sr) are also observed in such a plot, as shown previously by Lee (2005) and Chin et al. (2012), and were interpreted as evidence that the Big Creek peridotites interacted with fluids and/or hydrous melts. However, we cannot rule out the possibility that elevated Cs, Li, Ba, Rb, and Sr reflect recent metasomatism/contamination by the host lava.

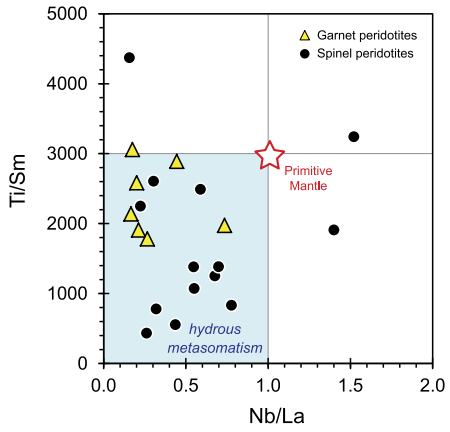

Fig. 4. Ti/Sm versus Nb/La ratios (ppm/ppm) of Sierran peridotites.

5.2. Oxygen isotope compositions of minerals

Oxygen isotope ratios for olivine, orthopyroxene, clinopyroxene, and garnet separates are reported in Table 1 and plotted in Fig. 5. The average $\delta^{18}O$ values of olivine in spinel peridotites ($n = 3$) and garnet peridotites ($n = 3$) are 5.2‰ and 5.3‰, respectively. The average $\delta^{18}O$ value of orthopyroxene in spinel peridotites is 6.1‰ and in garnet peridotite is 6.0‰. The average $\delta^{18}O$ value of clinopyroxene in spinel peridotite is 5.4‰ and in garnet peridotite is 5.6‰. These values are representative of typical mantle olivine (5.2‰), garnet (5.5‰), and orthopyroxene and clinopyroxene (5.6‰) (Deines and Haggerty, 2000). We also report $\delta^{18}O$ values of garnet from four garnet pyroxenites: BC98-7, BC98-5, BC98-9, and BCX. Samples BC98-7 and BC98-5 are high-MgO garnet pyroxenites, whereas BC98-9 and BCX are low-MgO garnet pyroxenites (Lee et al., 2006).

Reconstructed whole-rock $\delta^{18}O$ values, based on the average $\delta^{18}O$ values of different minerals and their modal abundance, in spinel and garnet peridotites range from 5.4 to 5.9‰. These whole-rock values overlap $\delta^{18}O$ values of typical mantle (~5.5 ± 0.2‰; Mattey et al., 1994; Eiler, 2001). In Fig. 5, we also plot for reference $\delta^{18}O$ values of minerals in peridotites interpreted to be metasomatized by slab-derived and/or carbonatitic melts (Perkins et al., 2006; Rehfeldt et al., 2008). The Sierran xenoliths mostly plot in the typical mantle field, although some samples, such as spinel peridotite 08BC13, extend into the "metasomatized" field.

Temperatures calculated based on equilibrium oxygen isotope exchange between clinopyroxene and olivine (Chiba et al., 1989) and orthopyroxene and olivine (Rosenbaum et al., 1994) support a high-temperature origin (>700 °C), with some temperatures as high as 1690 °C. In contrast, temperatures obtained using subsolidus mineral thermobarometry (Fe–Mg exchange between orthopyroxene and clinopyroxene coupled with Al net-transfer between orthopyroxene and garnet; (Brey and Kohler, 1990) are considerably lower, ranging from 670 to 870 °C (Chin et al., 2012)). Even if the high uncertainties associated with oxygen isotope temperatures (±200 °C; Chazot et al., 1997) compared to the Brey and Kohler thermobarometer (±20 °C) are taken into account, oxygen isotope temperatures are still considerably higher than those obtained using subsolidus mineral thermobarometry.

Substantial zoning in Al and Ca is observed in pyroxenes from the Big Creek peridotites (Lee et al., 2001a; Chin et al., 2012), and CaO-in-orthopyroxene thermometry (Brey and Kohler, 1990) of pyroxene cores yield higher "peak" temperatures between 900 and 1140 °C (Lee et al., 2001a) compared to temperatures obtained from rims. These features also support a high-temperature origin of the Sierran peridotites, followed by subsequent cooling rapid enough that the final mineral assemblage is in disequilibrium on the μm to mm scale. Thus, one possible explanation for the discrepancy between garnet-pyroxene thermobarometry and oxygen isotope thermometry is that in contrast to the small spot sizes (1 μm) used for garnet-pyroxene thermobarometry, laser fluorination is a bulk technique ablating several mineral grains simultaneously and therefore homogenizing any core–rim compositional disequilibrium. For the purposes of this study, any small oxygen isotope deviations from equilibrium are not significant.

6. Discussion

6.1. Sierran peridotites reflect a refertilization trend

Major element compositional trends observed in the Sierran peridotites (Fig. 3) appear consistent with those predicted for melt depletion from an originally fertile primitive mantle. However, simple melt depletion of canonical primitive mantle is difficult to reconcile with the anomalously high CaO and SiO_2 (corresponding to high modal abundances of clinopyroxene) observed in some

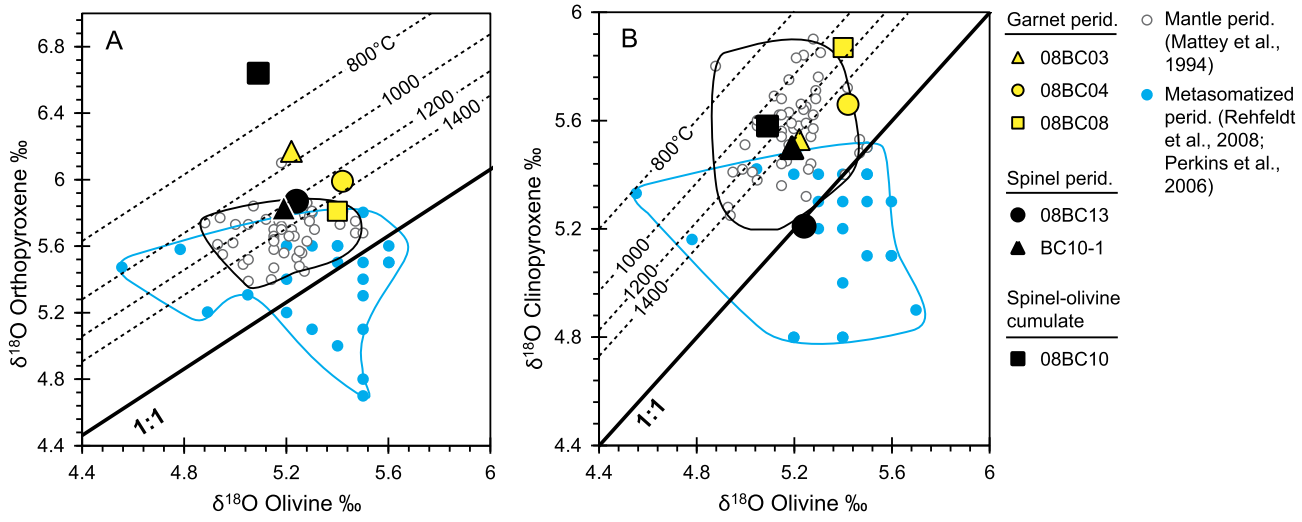

Fig. 5. $\delta^{18}O$ values of minerals from Sierran peridotites. A) $\delta^{18}O$ values in orthopyroxene vs. $\delta^{18}O$ values in olivine; B) $\delta^{18}O$ values in clinopyroxene vs. $\delta^{18}O$ values in olivine. Typical mantle peridotites from Mattey et al. (1994) and metasomatized peridotites from Rehfeldt et al. (2008) and Perkins et al. (2006) are also shown as white circles and blue circles, respectively. Temperature-dependent fractionation between minerals (dashed lines) are from Chiba et al. (1989) and Rosenbaum et al. (1994). (For interpretation of the references to color in this figure legend, the reader is referred to the web version of this article.)

of the Sierran garnet peridotites (Fig. 2B, Fig. 3A, D) as well as some spinel peridotites. These samples also have low MgO relative to primitive mantle and thus do not resemble typical residues, which would have elevated MgO relative to primitive mantle. Instead, several lines of evidence, as we discuss below, suggest that the Sierran peridotites may have had a melt component added back to it, a process which we refer to here as refertilization, as for example, described by Ionov et al. (2005), Le Roux et al. (2007) and Luffi et al. (2009).

In Fig. 3, we show batch melting curves (red lines) calculated using pMELTS (Ghiorso et al., 2002), beginning with a primitive mantle source (McDonough and Sun, 1995). Melting is modeled along an isentropic path initiating at 3 GPa and terminating at 0.3 GPa (assuming surface mantle potential temperature of 1300 °C). Also plotted are mixing lines (solid red, orange, and blue lines) between a melt-depleted peridotite (residue from 20% melting, corresponding to the most depleted spinel peridotites in terms of major elements) and three end-member mid-ocean ridge basalt (MORB) compositions, "H", "L", and "D" (Elthon, 1992). These MORB end-members approximate melts produced by decompression melting of upwelling mantle beneath mid-ocean ridges, with the "H" end-member corresponding to a low-F melt segregated at high pressures (2.5–3 GPa), followed by the "L" and "D" end-members which correspond to higher extents of melting with increased decompression. For CaO, Al_2O_3, and SiO_2, refertilization and melt depletion are for the most part indistinguishable. However, because Na is incompatible, it is rapidly depleted from the residue, resulting in concave upwards melting arrays in a plot of Na_2O versus MgO (Fig. 3C). Had melt extraction been assumed to be instantaneous (e.g., fractional melting), the melting array would be predicted to be even more non-linear owing to more efficient removal of Na. Thus the roughly linear trend displayed by the Sierran peridotites in Na_2O versus MgO is thus difficult to explain by melt depletion and may be better explained by mixing or reaction between a basaltic melt and a harzburgitic endmember as we discuss below. Re-introduction of basaltic melt and associated clinopyroxene precipitation would also explain the elevated CaO and SiO_2 (relative to primitive mantle) observed in garnet peridotites.

High Cr# (atomic $(Cr/(Cr+Al)) \times 100$) of relict spinels in combination with fertile bulk rock compositions may also suggest refertilization (Chin et al., 2012). Cr# in spinel is an indicator of the melting degree of mantle peridotites (Dick and Bullen, 1984), and increases with melting owing to the compatibility of Cr. Reintroduction of melt would decrease the whole-rock Cr#, but Cr# of relict, refractory spinel cores may survive post-melting phenomena (Voigt and von der Handt, 2011) and thus can preserve original melt depletion signatures. Cr# of spinel cores in both Sierran spinel peridotites and garnet peridotites range between 30 and 40, with the exception of two samples which have low (<20) Cr# spinel (Cr# of spinel rims in garnet peridotites has been increased relative to core compositions by garnet corona formation and thus only core compositions are of interest here). Cr#'s between 30 and 40 correspond to 15–20% melt depletion (Hirose and Kawamoto, 1995; Matsukage and Kubo, 2003). At these degrees of melting, modal clinopyroxene should be ~5% (Baker and Stolper, 1994). Some Sierran garnet peridotites, despite having high Cr# in relict spinel, have excess modal clinopyroxene (10–20%), which is greater than that predicted by simple melt depletion (Fig. 6). This suggests that the bulk rock has been refertilized, but the cores of spinels preserve a memory of prior melt depletion due to slow equilibration of Cr between spinel and whole-rock. The decoupling between Cr# in relict spinel and modal clinopyroxene in Fig. 6 is consistent with earlier findings of Chin et al. (2012), who showed similar decouplings between spinel Cr# and whole-rock composition. Major element compositional trends and high Cr# of relict

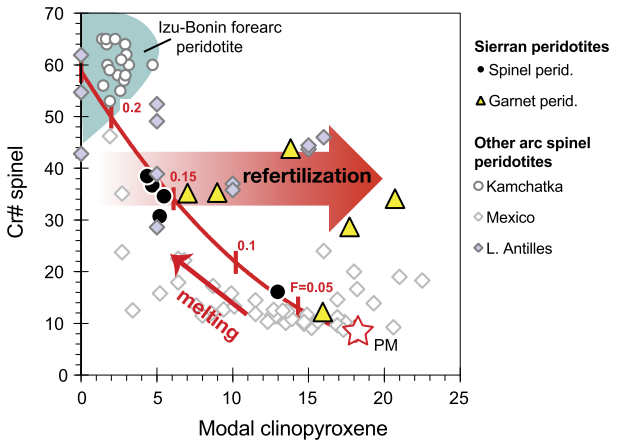

Fig. 6. Cr# (atomic $(Cr/(Cr+Al)) \times 100$) in spinel vs. clinopyroxene mode in Sierran peridotites. Data shown are from Lee et al. (2001a), Chin et al. (2012), and this study. Also plotted are spinel peridotites from Kamchatka (Ionov, 2010), Mexico (Liang and Elthon, 1990; Luhr and Aranda-Gomez, 1997; Blatter and Carmichael, 1998), and Lesser Antilles (Parkinson et al., 2003). Blue field represents peridotites from Izu Bonin (Parkinson and Pearce, 1998). (For interpretation of the references to color in this figure legend, the reader is referred to the web version of this article.)

spinel decoupled from modal clinopyroxene thus suggest a refertilization trend from a depleted harzburgitic precursor.

Based on thermobarometric constraints from our previous studies (Lee et al., 2001a; Chin et al., 2012), the extent of refertilization appears to increase with depth. Shallow depths (<90 km, 3 GPa) are dominated by undeformed, clinopyroxene-poor (<10%) spinel peridotites and smaller amounts of more fertile, clinopyroxene-rich (10–15%) spinel peridotites. At greater depths (90–110 km, 3–3.5 GPa) highly deformed garnet peridotites with excess clinopyroxene (>10%) are present. Chin et al. (2012) showed that the garnet peridotites originally formed as shallow spinel peridotites, which were subsequently transported to garnet facies depths and rapidly cooled, as evidenced by widespread preservation of mineral zonation and Al-depletion halos next to exsolved garnet and amphibole lamellae (Lee et al., 2001a; Chin et al., 2012). Based on their bulk rock compositions and their metamorphic histories, the Sierran peridotites have been interpreted to represent a cogenetic package of mantle lithosphere, initially formed by melt depletion associated with Mesozoic arc magmatism (Lee et al., 2001b) and then compressed and cooled as the lithosphere was thickened to pressures of 3–3.5 GPa, presumably approaching the top of the subducting slab (Chin et al., 2012).

Finally, although refertilization is most apparent in the garnet peridotites (e.g., excess clinopyroxene), both spinel and garnet peridotites were also affected by cryptic metasomatism, wherein the trace-element geochemistry appears to have been modified without concomitant changes in major elements or modal mineralogy. As shown in Fig. 4 and described earlier, both Sierran spinel peridotites and garnet peridotites have low Ti/Sm and Nb/La, but relative enrichment in large ion lithophile elements (LILE), such as Sr. We interpret the anomalously low Ti/Sm (<3000) and Nb/La (<1) ratios as indicating the involvement of a fluid metasomatic component, because of low solubility of Ti and Nb in fluids (Tatsumi et al., 1986). Interestingly, neither Sr/Nd nor U/Pb shows any systematic variation between the two lithologies, in contrast to the marked gradient in clinopyroxene mode with increasing pressure. Thus, the fluid-enriched signature of the Sierran xenoliths may represent a pervasive overprint, perhaps related to slab-derived fluids from the Farallon plate, as proposed by Lee (2005). Because the Farallon plate persisted beneath the Sierra Nevada arc long after arc magmatism ceased (Dumitru et al., 1991; Humphreys et al., 2003), it is not clear if this fluid signature was

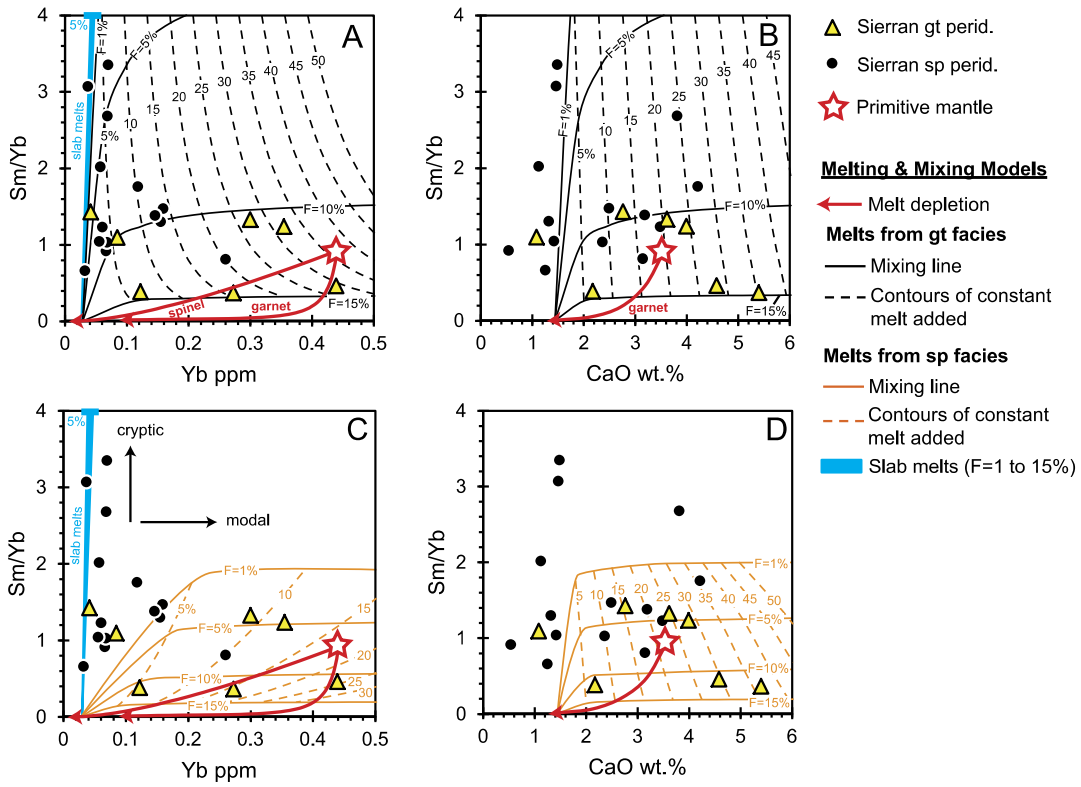

Fig. 7. Sm–Yb–CaO systematics of Sierran peridotites and binary mixing models (Sm and Yb in ppm and CaO in wt.%). Mixtures between 20% depleted primitive mantle and mantle-derived melts shown as solid colored lines (black for melts originating in the garnet facies; orange for melts originating in the spinel facies); contours of constant percentage of melt added to the depleted peridotite (5% increments) shown as dashed lines. Mixtures between depleted peridotite and slab melts (F ranging from 1 to 15%) plot in the blue fields in A) and C). Melt depletion curves (red lines) from primitive mantle (star) also shown for reference. The garnet and spinel facies melting curves are nearly identical for the Sm/Yb vs. CaO plots; thus only the garnet facies curve is shown. A) Sm/Yb versus Yb (ppm); melts originate from garnet facies B) Sm/Yb vs. CaO (wt.%); melts originate from garnet facies C) Sm/Yb versus Yb (ppm); melts originate from spinel facies D) Sm/Yb versus CaO (wt.%); melts originate from spinel facies. (For interpretation of the references to color in this figure legend, the reader is referred to the web version of this article.)

coeval with the major element refertilization or due to later metasomatism.

6.2. Refertilization models

In this section, we constrain the nature and extent of refertilization of the Sierran peridotites. How did the fertile garnet peridotites, which were demonstrated above to have originated as depleted spinel peridotites, come to contain excess clinopyroxene (and garnet), in contrast to the shallower spinel peridotites which appear to have experienced less refertilization? Was the refertilization related to infiltration of a slab melt or mantle melt? Here, we explore two end-member refertilization scenarios (Bodinier et al., 1988). The first scenario is that the refertilized peridotites represent a mixture between trapped melt and an original depleted harzburgite (batch melt addition). For example, clinopyroxene and garnet-enrichment in the mantle might be a product of high-pressure (>2 GPa) crystal fractionation of hydrous arc magmas (Green, 1972). The second scenario is that the refertilized peridotites represent products of melt-rock reaction between a passing melt and a peridotite protolith.

To evaluate these hypotheses, we modeled the behavior of trace elements because the major elements alone are not sufficient to distinguish between mixing and melt-rock reaction. We choose moderately incompatible trace elements because these elements are sensitive to mineralogic changes associated with refertilization, but rather insensitive to cryptic metasomatism (Canil, 2004; Lee et al., 2007a). MREEs and HREEs, in this regard, are useful because they are moderately incompatible and their partition coefficients are relatively well-constrained. We avoid the use of LREE because these elements are more susceptible to cryptic metasomatism (Nixon et al., 1981; Condie et al., 2004). In our models, we use Yb, which is sensitive to garnet growth, and Sm, which is more sensitive to clinopyroxene growth.

6.2.1. Binary mixing between melt and harzburgite

In Fig. 7, we show simple mixing models between a depleted peridotite precursor and various melts. In all mixing models, the depleted end-member is formed by 20% melt depletion of primitive mantle with composition of McDonough and Sun (1995), reflecting the most depleted Sierran spinel peridotites in terms of major element systematics (Fig. 3). This 20% depletion is also within the bounds estimated using Cr# of relict spinel cores, as described above and in Chin et al. (2012). To be consistent with the P–T path of the Sierran garnet peridotites interpreted by Chin et al. (2012), we assume that the depleted end-member originated in the spinel facies. To this depleted end-member peridotite, we add mantle-derived melts from both the spinel and garnet facies. Mixing with eclogite-derived melts was also modeled to simulate slab melt addition.

To model the trace element composition of mantle-derived melts and the initial composition of the depleted end-member residue, we used a non-modal, fractional melting model using starting mineral modes and melting modes from Johnson et al. (1990). Melts from the garnet stability field (black lines Fig. 7A, B) and spinel stability field (orange lines, Fig. 7C, D) were calculated. As mentioned above, a single depleted end-member formed in the spinel facies is used in all mixing scenarios. Slab-derived melts were calculated using an eclogitic source (62% garnet, 38% clinopyroxene) based on the melting relationships in Kessel et al. (2005).

Additional details on model set up can be found in the Supplemental Appendix 1.

For spinel-facies melting, Sm and Yb mineral/melt partition coefficients for clinopyroxene are from Hauri et al. (1994) and for olivine and orthopyroxene are from Lee et al. (2007a), the latter of which were determined so that they are internally consistent with the Hauri et al. (1994) clinopyroxene partition coefficients. Sm and Yb partition coefficients for spinel are from Stosch (1982). For garnet-facies melting, Yb mineral/melt partition coefficients for olivine, orthopyroxene, clinopyroxene, and garnet were taken from Canil (2004); Sm mineral/melt partition coefficients for olivine, orthopyroxene, and clinopyroxene were from Lee et al. (2007a) and for garnet from Johnson et al. (1990). Mineral/melt partition coefficients for eclogitic systems were taken from Barth et al. (2002). CaO contents of 1, 5, 10, and 15% melts of primitive mantle were obtained from the isentropic melting calculation described in Section 6.1. CaO in these mantle melts ranged from 5 to 12 wt.%.

In Fig. 7, mixing lines between the depleted peridotite end-member and mantle-derived melts corresponding to different melting fractions ($F = 1$–15%) are plotted as solid lines; dashed lines represent contours of 5% melt increments added to the mixture. In Fig. 7A and B, mixing of depleted peridotite with melts derived from the garnet facies is shown, whereas in Fig. 7C and D, mixing with spinel peridotite melts is shown. Melt depletion trends predicted for residual peridotite are also shown for comparison (red lines).

The results of these models can be summarized as follows. Melt depletion results in depletion in Sm and Yb, but greater depletion in Sm compared to Yb and CaO because CaO and Yb are less incompatible than Sm. This results in concave up positive correlations of Sm/Yb versus Yb and CaO during melting. Mixing, however, gives fundamentally different trends. Mixing with mantle-derived melts gives convex upwards mixing lines in Sm/Yb versus Yb or CaO diagrams because the relative enrichment of Sm in mantle melts is far higher than that of Yb and Ca. Due to the differences in compatibility of these elements, the addition of low degree melts will increase Sm/Yb at a rate faster than Yb or Ca, increasing the nonlinearity of the mixing curves. In detail, because melts derived from garnet peridotite melting have significantly lower Yb than melts derived from spinel peridotites, mixing with garnet peridotite melts causes a greater increase in Sm/Yb for the same amount of mixing with a spinel peridotite melt. Finally, because of the large amount of garnet (>50%) in the residue of slab melts, Yb behaves as a compatible element during slab melting, generating hypothetical melts with extremely high Sm/Yb. This results in nearly vertical mixing lines in Sm/Yb versus Yb plots.

With the understanding of these trends in place, we can now examine the Sierran peridotites. The spinel peridotites have variable Yb and CaO, but some have anomalously high Sm/Yb compared to the garnet peridotites. The garnet peridotites have variable Yb and CaO, but are generally higher in Yb and CaO than the spinel peridotites. In particular, the Sm/Yb ratios of the garnet peridotites show no correlation with Yb or CaO. Some of the spinel and garnet peridotites overlap in composition. There appears to be no strong evidence that the peridotites have mixed with any significant amount (e.g., >5%) of a slab melt. While four of the spinel peridotites have Sm–Yb systematics consistent with small amounts of added slab melt, these samples can also be explained by the addition of low-degree garnet peridotite melts, resulting in cryptic metasomatism. For the rest of the peridotites, it can be seen that the Sm–Yb–CaO systematics of both the spinel and garnet peridotites can be explained by mixing of up to 30% of a 10–15% melt of a garnet peridotite or 15–30% of a 5–10% melt of a spinel peridotite (Fig. 7). Assuming clinopyroxene has a CaO content of ~20 wt.% and that the mantle melts have ~10% CaO and assuming that all the CaO in the added melt is eventually accounted for by clinopyroxene, such mixing proportions of melt correspond to the addition of ~7–17% of clinopyroxene added to the harzburgite. Although this mixing scenario is simplistic, the estimated amount of clinopyroxene added is consistent with the observed mineral modes.

6.2.2. Melt-rock reaction

We now examine the second refertilization scenario: melt-rock reaction. Here, a passing melt reacts with a protolith, leaving behind a reacted rock that has partially or fully equilibrated with, but no longer contains, the melt. Depending on the melt/rock ratio, the extent of equilibration between melt and rock, and the compositions of melts and harzburgitic precursors, melt-rock reaction can generate a diversity of reacted rock types (Garrido and Bodinier, 1999). We model the end-member case where the melt is in excess and the protolith compositionally equilibrates with the melt, resulting in an increase in clinopyroxene along with a change in trace element composition. In other words, we assume the melt/rock ratio is so high that the melt does not change its composition, but the major and trace element composition of the rock changes accordingly. In this model, we evaluate the extreme case in which the observed mineralogy represents the product of melt-rock reaction rather than mixing, and our goal is to quantify how this reaction is manifested in whole-rock trace element composition. Although this approach is simplistic, it bounds the geochemical modification of peridotites by melt-rock reaction.

In our model, the reacted mineral compositions are constrained by the equilibrium partition coefficient. We use the garnet-facies melt compositions (1, 5, 10, and 15% melts of primitive mantle) from the mixing calculations discussed in the previous section (Fig. 7). We assume that the observed mineral modes are already the product of refertilization. Our goal is to calculate the trace element signature of the peridotites upon equilibration with the melt. For a given melt composition and known partition coefficients (see above), we calculate olivine, orthopyroxene, clinopyroxene, and garnet trace element compositions in equilibrium with the melt. Hypothetical bulk rock compositions are then estimated with a weighted average of all the minerals according to their observed modes. To explore the plausible variable space so that the entire spectrum of peridotites is encompassed, we generated two hypothetical arrays. In one, we varied clinopyroxene mode from zero to 100%, keeping the olivine/orthopyroxene ratio constant at 2. In the second array, we varied garnet mode while keeping clinopyroxene/olivine and clinopyroxene/orthopyroxene ratios fixed at 0.15 and 0.2, respectively. For further details on the model setup, the reader is referred to Supplemental Appendix 1.

In Fig. 8, we summarize our model results. When only clinopyroxene is varied, the suites of reacted rocks follow positive, concave down trajectories on a plot of Sm/Yb versus Yb (Fig. 8A), superficially resembling binary mixing (Fig. 7A). An additional feature of the Sm/Yb versus Yb plot in Fig. 8A is that rocks reacted with low-F melts fall on highly non-linear trends compared to rocks reacted with higher F melts. This is because clinopyroxenes in equilibrium with low-F melts have higher Sm/Yb compared to clinopyroxenes in equilibrium with high-F melts, in which Sm is diluted.

When garnet is varied, the reaction arrays in the Sm/Yb versus Yb plots have negative slopes and are concave up (Fig. 8B) compared to the clinopyroxene-only case. Sm/Yb ratios in reacted rocks decrease with increasing garnet mode, owing to the compatibility of Yb in garnet. Finally, isopleths of clinopyroxene and garnet mode in Fig. 7 have negative slopes because the concentrations of Sm and Yb in the melts decrease and increase, respectively, with increasing F for garnet-facies melting.

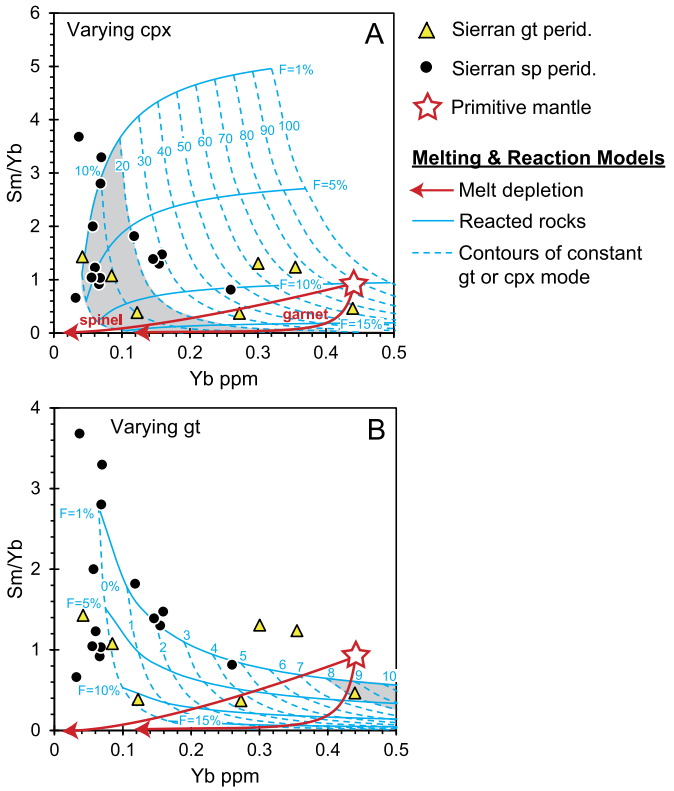

Fig. 8. Sm–Yb systematics of Sierran peridotites and melt-rock reaction models. Arrays of reacted rocks are shown as solid blue lines. Contours of constant clinopyroxene (cpx) mode or garnet (gt) mode shown as dashed blue lines. Melt depletion curves (red lines) from primitive mantle (star) also shown for reference. Gray field represents range of observed modal clinopyroxene or garnet in the Sierran peridotites. A) Sm/Yb versus Yb (ppm), varying clinopyroxene mode while olivine/orthopyroxene ratio fixed at 2 in reacted rocks. B) Sm/Yb versus Yb (ppm); varying garnet mode while clinopyroxene/olivine = 0.15 and clinopyroxene/orthopyroxene =0.2. (For interpretation of the references to color in this figure legend, the reader is referred to the web version of this article.)

We now compare the Sierran peridotite compositions to the hypothetical melt-rock reaction arrays. As an additional constraint, we also denote the field (gray), which corresponds to the observed range of clinopyroxene (Fig. 8A) and garnet (Fig. 8B) modes in the Sierran peridotites. In Fig. 8A, half of the spinel peridotites fall within the gray field, suggesting they could represent reacted rocks containing 10% or less modal clinopyroxene and reacted with low F (1–5%) melts. However, some spinel peridotites cannot be explained as melt-rock reaction products because to fit their Sm/Yb systematics would require reaction with modal clinopyroxene (>30%) higher than observed. Similarly, to fit the Sm/Yb of most of the garnet peridotites would require reaction with protoliths having >50% modal clinopyroxene, far higher than observed. If we examine the models where garnet mode is varied, even fewer data can be explained as melt-rock reaction products (only one sample falls within the gray field in Fig. 8B). Several garnet peridotites plot above the trend of rocks reacted with a low-F melt. In summary, melt-rock reaction at best explains a small subset of the observed trace element compositions. The variable clinopyroxene model (Fig. 8A) can only reproduce trace element signatures with unreasonably high clinopyroxene modes, and the variable garnet model (Fig. 8B) fails to explain the majority of garnet peridotites (except for one sample). The simplest model for explaining the major and trace element systematics of the Sierran peridotites is thus binary mixing, that is, the addition of a melt to a depleted peridotite.

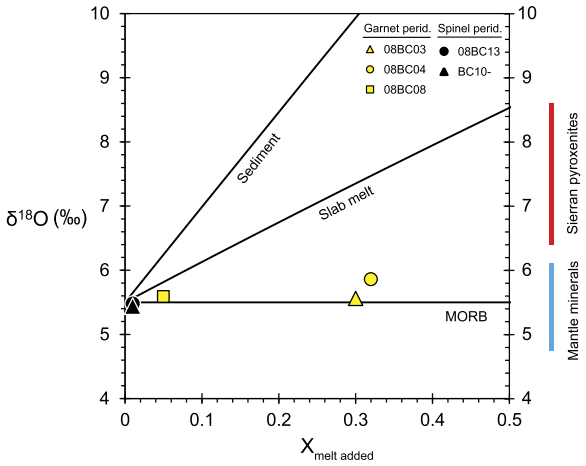

Fig. 9. Reconstructed bulk δ^{18}O value of Sierran peridotites versus fraction of melt added based on batch addition model (see Fig. 6). Mixing end-members sediment (pelagic clay with a δ^{18}O value of 20‰ from Clayton et al., 1972, and slab melt with a δ^{18}O value of 11.3‰ from Eiler et al., 1998) also shown. Field of Sierran pyroxenites is from Ducea (2002) and field labeled "mantle minerals" from Mattey et al. (1994).

6.3. Constraints on origin of the refertilizing melt from oxygen isotopes

A key question is whether the refertilizing magmas are mantle-derived melts or slab melts. In our above discussion of Sm–Yb–CaO systematics, the contribution of slab melts to major element refertilization was considered to be small or negligible (<5%). Oxygen isotopes can provide additional constraints on the origin of the refertilizing magmas. In particular, because O is a major element, any observed changes in bulk rock O isotopes require significant amounts of open system behavior.

In Fig. 9, we compare the reconstructed bulk δ^{18}O value of the Sierran peridotites to hypothetical mixing lines between mantle harzburgite (5.5‰) and three melt endmembers: mid-ocean ridge basalt (MORB; 5.5‰), a slab melt (11.3‰; Eiler et al., 1998), and pelagic clay (20‰, Clayton et al., 1972; Savin and Epstein, 1970). The slab melt composition from Eiler et al. (1998) was chosen because as a trapped melt inclusion in a mantle olivine xenocryst, this melt might approximate a pristine slab-derived melt undisturbed by any crustal contamination. In addition, the pelagic clay average of 20‰ was selected as a lower limit of the spectrum of oceanic sediments (marine carbonates and cherts would have even higher δ^{18}O values: 25–32‰ and 35–42‰, respectively; Kolodny and Epstein, 1976).

In Fig. 9, we plot bulk δ^{18}O value versus estimated amount of melt added. To change bulk the δ^{18}O value significantly requires the addition of large amounts of melt, which would be reflected in high clinopyroxene mode. Samples with high clinopyroxene mode have mantle-like δ^{18}O values. Thus, it is clear that the Sierran peridotites are best explained as mixtures with mantle-derived melts, such as MORB, not with endmembers with anomalously high δ^{18}O values because the bulk δ^{18}O value is indistinguishable from mantle values to within error of our measurements and natural variation of unmetasomatized mantle rocks.

6.4. Timing of refertilization

Although absolute age constraints are unavailable for the Sierran peridotites, we can still narrow down when refertilization was likely to have occurred based on the nature of the melt infiltration event, patterns of chemical zonation in minerals, and regional geologic context. Our binary mixing model in Section 6.2.1, combined with oxygen isotope data in Section 6.3, show that refertilizing melt was derived from the mantle, not the subducting slab. Thus,

refertilization had to have occurred while asthenospheric mantle was still present beneath the Sierras – at high temperatures at or above the mantle solidus (>1000 °C). There were two periods in Western US geologic history when asthenospheric mantle was present beneath the Sierras: 1) during arc magmatism in the Mesozoic, and 2) during the slab window opening in the Cenozoic.

Despite the deep (3–3.5 GPa, or 90–105 km) and cold (670–870 °C) final equilibration P-T of the garnet peridotites, their high degree of melt depletion (15–20%), high Al in orthopyroxene cores, and low whole-rock HREE concentrations argue against melt depletion at 3–3.5 GPa, because anhydrous decompression melting at these pressures would correspond to unusually high mantle Tp (Chin et al., 2012). Instead, Chin et al. interpreted a P–T path where the (now garnet) peridotites were originally melt-depleted in the spinel facies, and were then transported into the garnet facies, where the peridotites were cooled. Equilibration at ~3 GPa approaches the average depth to the slab (Tatsumi, 1986), and thus cooling due to slab impingement can explain the observed zonation in pyroxenes from high Al and Ca cores to low Al and Ca rims, as well as the presence of late-stage amphibole lamellae (Lee et al., 2001a; Chin et al., 2012). Sm–Nd ages on garnet pyroxenites that equilibrated within the same P–T interval as garnet peridotites also indicate that the ~100 km root was in place by the time of peak Late Cretaceous arc magmatism (Ducea and Saleeby, 1998). Residence of the peridotites in the vicinity of a slab is also supported by the peridotites' whole-rock trace element geochemistry, which shows enrichments in fluid-mobile elements and depletion in high-field strength elements.

Based on the above, the Sierran peridotites were most likely refertilized during Mesozoic arc magmatism. Refertilization occurred prior to the peridotites' reaching their final equilibration P–T at ~3 GPa and from 670 to 870 °C, conditions approaching the slab top. It is unlikely that the peridotites were refertilized as a result of asthenospheric influx due to slab window opening in the Cenozoic. If that were the case, we would expect to see evidence of heating (e.g., high Al, Ca pyroxene rims), re-set Sm–Nd ages, and lack of a distinctive "subduction zone" trace element signature in the whole rocks. Instead, we suggest that the opening of the slab window was more likely the trigger for the deep-seated eruption that entrained the cold overlying lithosphere as xenoliths in the Late Miocene.

6.5. The deep lithosphere filter in global arcs

We showed that the Sierran mantle lithosphere, particularly the deepest garnet peridotites, experienced pervasive refertilization by basaltic, mantle-derived melts rather than slab-derived melts. In contrast, most shallow spinel peridotites experienced smaller degrees of refertilization. Both spinel and garnet peridotites also record a cryptic metasomatic overprint, with enriched LILE and depleted HFSE in whole-rocks, probably related to the long-lived Farallon slab beneath the Western USA.

To explain the depth-gradation in refertilization, we propose the following scenario (Fig. 1). Where mantle lithosphere is thick, as in continental arcs such as the Sierra Nevada, we hypothesize that the longer crustal and lithospheric column more efficiently traps rising magmas, resulting in refertilization of the deeper portions of the mantle lithosphere and manifesting as the addition of clinopyroxene. The deepest arc garnet peridotites thus appear anomalously fertile. We hypothesize that, in arcs with thin lithosphere (e.g., most island arcs), melts are granted easier passage and thus are not trapped as efficiently within the crust or lithospheric mantle. These shallow peridotites are thus predicted to show less refertilization. However, shallow peridotites may still be affected by cryptic metasomatism.

Our hypothesis predicts that there should be a contrast in major element fertility of the lithospheric mantle underlying oceanic island arcs and continental arcs, with continental arc lithospheric mantle being more fertile because they are generally underlain by thicker crust, and by implication, thicker lithosphere. In Fig. 3, we plot global peridotites from various arcs and back-arcs. Adopting Gill's (1981) classification, we define arcs as "juvenile" if they have crust <25 km thick and arcs as "mature" if they have crust >25 km thick. Crustal thickness does not equate with lithosphere thickness, but we assume that thick crust implies thicker lithosphere in tectonically active areas.

Juvenile arcs for which peridotite xenolith data are available include Izu Bonin (Parkinson and Pearce, 1998), South Sandwich (Pearce et al., 2000), and Simcoe Volcanic Field in the Cascade backarc (Brandon and Draper, 1996). Crustal thicknesses of the Izu Bonin and South Sandwich arc are estimated to be 22 km and 20 km, respectively (Takahashi et al., 1998; Larter et al., 2003). We consider Simcoe "juvenile" based on crustal thickness estimates between 20 and 30 km in the neighboring Columbia Plateau region (Hill, 1972; Catchings and Mooney, 1988). Mature arcs with available peridotite xenolith data include Mexico (Liang and Elthon, 1990; Luhr and Aranda-Gomez, 1997; Blatter and Carmichael, 1998), Kamchatka (Ionov, 2010), the Ichinomegata Crater on Honshu (Canil, 2004), Canadian Cordillera (Peslier et al., 2002), the Philippines (Maury et al., 1992), and the Lesser Antilles (Parkinson et al., 2003). Crustal thicknesses for these arcs are: Mexico, 35–50 km (Urrutia-Fucugauchi and Flores-Ruiz, 1996); Kamchatka, 30–40 km (Levin et al., 2002); Ichinomegata, 30–35 km (Taira, 2001); Canadian Cordillera, 35–40 km (Cook et al., 1988); Philippines, 34 km (Besana et al., 1995); and Lesser Antilles, 33 km (Boynton et al., 1979).

From Fig. 3, it is apparent that mature arcs (including the Sierran peridotites), span the entire spectrum from depleted to fertile compositions, with some arcs containing peridotites even more fertile than primitive mantle. Similar to the Sierran xenoliths, peridotites from the Lesser Antilles were interpreted by Parkinson and Pearce (1998) as refertilized, clinopyroxene-enriched harzburgites. The Mexican arc also contains some highly fertile peridotites, but whether these have been refertilized by recent arc magmatism or are remnants of non-arc mantle from the distant past is unclear, given the long and complex tectonic history in that region. In contrast to the mature arcs, very few peridotites from juvenile arcs extend to highly fertile compositions, with the majority plotting at the melt-depleted end. However, one caveat to bear in mind is that the peridotites from juvenile arcs (e.g., Izu Bonin and South Sandwich) are from the forearc, and thus it is not clear whether they are truly residual mantle associated with arc magmatism or accreted oceanic lithosphere that was subsequently modified by subduction processes.

Although the number of peridotites sampled at mature arcs outnumbers those from juvenile arcs based on the literature data shown in Fig. 3, lithospheric mantle beneath mature arcs seem to trend towards higher fertility than beneath juvenile arcs. Higher fertility, particularly in CaO, could be the result of refertilization by melt entrapment and high-pressure clinopyroxene fractionation, similar to what is observed in the Sierran peridotites. That this trend is observed in the global data supports our hypothesis that thicker arcs could cause primary arc magmas to fractionate within the lithospheric mantle and therefore before rising across the Moho and into the crust. Mafic minerals such as garnet, amphibole, and pyroxenes comprise deep crustal cumulates of arc magmas, and fractionation of these minerals is considered one mechanism by which primitive magmas evolve to granitoid compositions (Ducea, 2001; Greene et al., 2006; Lee et al., 2006; Müntener and Ulmer, 2006; Alonso-Perez et al., 2009; Jagoutz et al., 2009). Our observations suggest that magmas may fractionate

clinopyroxene well before entering the crust. Such fractionation would increase Al and decrease Ca without significant change in SiO_2 in the magma, generating an evolved basalt from which all shallower fractionation in the crust must derive.

7. Conclusions

Peridotite xenoliths from the Sierra Nevada reveal a depth-gradation in refertilization from depleted spinel peridotite at depths < 90 km to fertile garnet peridotites between depths of 90 and 105 km. Textural, modal and geochemical observations show that spinel peridotites are undeformed, clinopyroxene-poor, and generally depleted in magmaphile elements (CaO, Na_2O), whereas garnet peridotites are highly deformed, clinopyroxene-rich, and have fertile major element compositions, with some garnet peridotites even more fertile than canonical primitive mantle. High Cr# of relict spinels in the garnet peridotites suggest that the garnet peridotites were original depleted spinel peridotites that were subsequently refertilized. The simplest explanation for the observed refertilization trends is that the fertile Sierran peridotites represent binary mixtures between a depleted spinel peridotite and up to 30% of a mantle-derived melt. As such, refertilization temperatures had to have been as high as that of ambient convecting mantle, suggesting that refertilization was concomitant with Mesozoic arc magmatism rather than the Laramide Orogeny (70–40 Ma), when lithospheric temperatures were cold and a mantle wedge was absent beneath the arc (Dumitru et al., 1991; Bird, 1988). It is unlikely that opening of the slab window at 10–15 Ma caused refertilization. Inflow of asthenosphere associated with the slab window should cause heating of the deep lithosphere, but abundant evidence for cooling (zoned pyroxenes, garnet exsolution) is preserved in deep lithospheric xenoliths.

Our study provides some new insights into the nature of metasomatism in a continental arc setting. We show that the residual arc mantle is refertilized while the arc is still magmatically active, and that the source of refertilizing melts is from the mantle itself rather than the subducting slab. However, evidence of slab metasomatism is observed as a ubiquitous cryptic overprint (enriched LILE, depleted HFSE) in all Sierran peridotites, probably owing to the prolonged residence of the Farallon slab beneath the Western US. In many island arcs worldwide, the slab has been implicated as the primary source for both cryptic and modal metasomatism (Maury et al., 1992; Kepezhinskas et al., 1996; McInnes et al., 2001). Here, we show that the mantle wedge also contributes a significant modal metasomatic component to the deep arc lithosphere. We suggest that thicker mantle lithosphere, a feature of most mature continental arcs, facilitates entrapment of primary mantle-derived melts at depth, resulting in a refertilized, clinopyroxene-enriched mantle. In contrast, the thinner lithosphere beneath most juvenile island arcs prevents deep melt entrapment, thus only preserving the cryptic slab component.

Comparison to mantle xenoliths from other arc environments suggests that refertilization of arc lithospheric mantle may be an important process associated with arc magmatism. The global arc peridotite data shows a general trend towards higher fertility in mature arcs with thick crust compared to juvenile arcs with thin crust. Significant sub-Moho magmatic fractionation may thus occur beneath mature arcs, implying that “primary” arc magmas may undergo high-pressure fractionation before they reach the crust.

Acknowledgements

This work was supported by NSF EAR-1119315 to Lee and Chin and a Geological Society of America Grant in Aid of Research to Chin. T. Larson is thanked for help with stable isotope data collection. We thank T. Plank for referring us to literature sources for crustal thicknesses of global arcs. We also thank M. Tice for help with micro-XRF mapping of thin sections. Finally, we thank Mihai Ducea and an anonymous reviewer for constructive reviews that greatly improved the manuscript.

Appendix A. Supplementary material

Supplementary material related to this article can be found online at http://dx.doi.org/10.1016/j.epsl.2014.04.022.

References

Alonso-Perez, R., Müntener, O., Ulmer, P., 2009. Igneous garnet and amphibole fractionation in the roots of island arcs: experimental constraints on andesitic liquids. Contrib. Mineral. Petrol. 157, 541–558.
Annen, C., Blundy, J.D., Sparks, R.S.J., 2006. The genesis of intermediate and silicic magmas in deep crustal hot zones. J. Petrol. 47, 505–539.
Atwater, T., 1970. Implications of plate tectonics for the Cenozoic tectonic evolution of Western North America. Geol. Soc. Am. Bull. 81, 3513–3536.
Atwater, T., Stock, J., 1998. Pacific–North America plate tectonics of the Neogene southwestern United States: an update. Int. Geol. Rev. 40, 375–402.
Baker, M.B., Stolper, E.M., 1994. Determining the composition of high-pressure mantle melts using diamond aggregates. Geochim. Cosmochim. Acta 58, 2811–2827.
Barth, M.G., Foley, S.F., Horn, I., 2002. Partial melting in Archean subduction zones: constraints from experimentally determined trace element partition coefficients between eclogitic minerals and tonalitic melts under upper mantle conditions. Precambrian Res. 113, 323–340.
Barton, M.D., 1996. Granitic magmatism and metallogeny of southwestern North America. In: Brown, M., Candela, P.A., Peck, D.L., Stephens, R.J.W., Zen, E.-A. (Eds.), The Third Hutton Symposium on the Origin of Granites and Related Rocks. In: GSA Special Papers, pp. 261–280.
Besana, G.M., Shibutani, T., Hirano, N., Ando, M., Bautista, B., Narag, I., Punongbayan, R.S., 1995. The shear wave velocity structure of the crust and uppermost mantle beneath Tagaytay, Philippines inferred from receiver function analysis. Geophys. Res. Lett. 22, 3143–3146.
Bird, P., 1988. Formation of the Rocky Mountains, Western United States: a continuum computer model. Science 239, 1501–1507.
Blatter, D.L., Carmichael, I.S.E., 1998. Hornblende peridotite xenoliths from central Mexico reveal the highly oxidized nature of subarc upper mantle. Geology 26, 1035–1038.
Blatter, D., Sisson, T., Hankins, W.B., 2013. Crystallization of oxidized, moderately hydrous arc basalt at mid- to lower-crustal pressures: implications for andesite genesis. Contrib. Mineral. Petrol. 166, 861–886.
Bodinier, J.L., Dupuy, C., Dostal, J., 1988. Geochemistry and petrogenesis of Eastern Pyrenean peridotites. Geochim. Cosmochim. Acta 52, 2893–2907.
Bohrson, W.A., Spera, F.J., 2001. Energy-constrained open-system magmatic processes II: application of energy-constrained assimilation–fractional crystallization (EC-AFC) model to magmatic systems. J. Petrol. 42, 1019–1041.
Bowen, N.L., 1928. The Evolution of the Igneous Rocks. Dover Publications, Inc., New York.
Boynton, C.H., Westbrook, G.K., Bott, M.H.P., Long, R.E., 1979. A seismic refraction investigation of crustal structure beneath the Lesser Antilles island arc. Geophys. J. R. Astron. Soc. 58, 371–393.
Brandon, A.D., Draper, D.S., 1996. Constraints on the origin of the oxidation state of mantle overlying subduction zones: an example from Simcoe, Washington, USA. Geochim. Cosmochim. Acta 60, 1739–1749.
Brey, G.P., Kohler, T., 1990. Geothermobarometry in four-phase lherzolites II. New thermobarometers, and practical assessment of existing thermobarometers. J. Petrol. 31, 1353–1378.
Canil, D., 2004. Mildly incompatible elements in peridotites and the origins of mantle lithosphere. Lithos 77, 375–393.
Catchings, R.D., Mooney, W.D., 1988. Crustal structure of the Columbia Plateau: evidence for continental rifting. J. Geophys. Res., Solid Earth 93, 459–474.
Chaussard, E., Amelung, F., 2012. Precursory inflation of shallow magma reservoirs at west Sunda volcanoes detected by InSAR. Geophys. Res. Lett. 39 (21), 1–6.
Chazot, Gilles, et al., 1997. Oxygen isotopic composition of hydrous and anhydrous mantle peridotites. Geochim. Cosmochim. Acta 61 (1), 161–169.
Chen, J.H., Moore, J.G., 1982. Uranium–lead isotopic ages from the Sierra Nevada batholith, California. J. Geophys. Res. 87, 4761–4784.
Chen, C., Presnall, D., 1975. The system Mg_2SiO_4–SiO_2 at pressures up to 25 kilobars. Am. Mineral. 60, 398–406.
Chiba, H., Chacko, T., Clayton, R.N., Goldsmith, J.R., 1989. Oxygen isotope fractionations involving diopside, forsterite, magnetite, and calcite: application to geothermometry. Geochim. Cosmochim. Acta 53, 2985–2995.
Chin, E.J., Lee, C.-T.A., Luffi, P., Tice, M., 2012. Deep lithospheric thickening and refertilization beneath continental arcs: case study of the P, T and compositional evolution of peridotite xenoliths from the Sierra Nevada, California. J. Petrol. 53, 477–511.

Chin, E.J., Lee, C.-T.A., Tollstrup, D.L., Xie, L., Wimpenny, J.B., Yin, Q.-Z., 2013. On the origin of hot metasedimentary quartzites in the lower crust of continental arcs. Earth Planet. Sci. Lett. 361, 120–133.
Clayton, R.N., Rex, R.W., Syers, J.K., Jackson, M.L., 1972. Oxygen isotope abundance in quartz from Pacific pelagic sediments. J. Geophys. Res. 77, 3907–3915.
Coleman, D.S., Glazner, A.F., 1997. The Sierra Crest magmatic event: rapid formation of juvenile crust during the late Cretaceous in California. Int. Geol. Rev. 39, 768–787.
Condie, K.C., Cox, J.O., O'Reilly, S.Y., Griffin, W.L., Kerrich, R., 2004. Distribution of high field strength and rare earth elements in mantle and lower crustal xenoliths from the southwestern United States: the role of grain-boundary phases. Geochim. Cosmochim. Acta 68, 3919–3942.
Coney, P.J., Reynolds, S.J., 1977. Cordilleran Benioff zones. Nature 270, 403–406.
Cook, F.A., Green, A.G., Simony, P.S., Price, R.A., Parrish, R.R., Mikereit, B., Gordy, P.L., Brown, R.L., Coflin, K.C., Patenaude, C., 1988. Lithoprobe seismic reflection structure of the southeastern Canadian Cordillera: initial results. Tectonics 7, 157–180.
DeCelles, P.G., Ducea, M.N., Kapp, P., Zandt, G., 2009. Cyclicity in Cordilleran orogenic systems. Nat. Geosci. 2, 251–257.
Deines, P., Haggerty, S.E., 2000. Small-scale oxygen isotope variations and petrochemistry of ultradeep (>300 km) and transition zone xenoliths. Geochim. Cosmochim. Acta 64, 117–131.
DePaolo, D.J., 1981. A neodymium and strontium isotopic study of the Mesozoic calc-alkaline granitic batholiths of the Sierra Nevada and Peninsular Ranges, California. J. Geophys. Res., Solid Earth 86, 10470–10488.
Dick, H.J.B., Bullen, T., 1984. Chromian spinel as a petrogenetic indicator in abyssal and alpine-type peridotites and spatially associated lavas. Contrib. Mineral. Petrol. 86, 54–76.
Dickinson, W.R., Snyder, W.S., 1978. Plate tectonics of the Laramide orogeny. In: Matthews, V. (Ed.), Laramide Folding Associated with Basement Block Faulting in the Western United States. In: Mem. Geol. Soc. Amer., vol. 151, pp. 355–366.
Dickinson, W.R., Snyder, W.S., 1979. Geometry of subducted slabs related to San Andreas transform. J. Geol. 87, 609–627.
Dodge, F.C.W., Lockwood, J.P., Calk, L.C., 1988. Fragments of the mantle and crust from beneath the Sierra Nevada batholith: xenoliths in a volcanic pipe near Big Creek, California. Geol. Soc. Am. Bull. 100, 938–947.
Ducea, M.N., 2001. The California arc: thick granitic batholiths, eclogitic residues, lithospheric-scale thrusting, and magmatic flare-ups. GSA Today 11, 4–10.
Ducea, M.N., 2002. Constraints on the bulk composition and root foundering rates of continental arcs: a California arc perspective. J. Geophys. Res. 107, 2304.
Ducea, M.N., Saleeby, J.B., 1996. Buoyancy sources for a large, unrooted mountain range, the Sierra Nevada, California: evidence from xenolith thermobarometry. J. Geophys. Res. 101, 8229–8244.
Ducea, M.N., Saleeby, J.B., 1998. The age and origin of a thick mafic–ultramafic keel from beneath the Sierra Nevada batholith. Contrib. Mineral. Petrol. 133, 169–185.
Dufek, J., Bachmann, O., 2010. Quantum magmatism: magmatic compositional gaps generated by melt-crystal dynamics. Geology 38, 687–690.
Dumitru, T.A., Gans, P.B., Foster, D.A., Miller, E.L., 1991. Refrigeration of the western Cordilleran lithosphere during Laramide shallow-angle subduction. Geology 19, 1145–1148.
Eggins, S.M., Woodhead, J.D., Kinsley, L.P.J., Mortimer, G.E., Sylvester, P., McCulloch, M.T., Hergt, J.M., Handler, M.R., 1997. A simple method for the precise determination of >40 trace elements in geological samples by ICPMS using enriched isotope internal standardisation. Chem. Geol. 134, 311–326.
Eiler, J., 2001. Oxygen isotope variations in basaltic lavas and upper mantle rocks. In: Valley, J.W., Cole, D.R. (Eds.), Stable Isotope Geochemistry. In: Rev. Mineral. Geochem., vol. 43. Mineralogical Society of America, Washington, DC, pp. 319–364.
Eiler, J.M., McInnes, B., Valley, J.W., Graham, C.M., Stolper, E.M., 1998. Oxygen isotope evidence for slab-derived fluids in the sub-arc mantle. Nature 393, 777–781.
Elthon, D., 1992. Chemical trends in abyssal peridotites: refertilization of depleted suboceanic mantle. J. Geophys. Res. 97, 9015–9025.
Farmer, G.L., Glazner, A.F., Manley, C.R., 2002. Did lithospheric delamination trigger late Cenozoic potassic volcanism in the southern Sierra Nevada, California? Geol. Soc. Am. Bull. 114, 754–768.
Feldstein, S.N., Lange, R.A., 1999. Pliocene potassic magmas from the Kings River region, Sierra Nevada, California: evidence for melting of a subduction-modified mantle. J. Petrol. 40, 1301–1320.
Fliedner, M.M., Ruppert, S., 1996. Three-dimensional crustal structure of the southern Sierra Nevada from seismic fan profiles and gravity modeling. Geology 24 (4), 367–370.
Garrido, C.J., Bodinier, J.-L., 1999. Diversity of mafic rocks in the Ronda peridotite: evidence for pervasive melt-rock reaction during heating of subcontinental lithosphere by upwelling asthenosphere. J. Petrol. 40, 729–754.
Ghiorso, M.S., Hirschmann, M.M., Reiners, P.W., Kress, V.C., 2002. The pMELTS: a revision of MELTS for improved calculation of phase relations and major element partitioning related to partial melting of the mantle to 3 GPa. Geochem. Geophys. Geosyst. 3, 1–35.
Gill, J.B., 1981. Orogenic Andesites and Plate Tectonics. Springer-Verlag, Berlin.
Green, T., 1972. Crystallization of calc-alkaline andesite under controlled high-pressure hydrous conditions. Contrib. Mineral. Petrol. 34, 150–166.
Greene, A.R., DeBari, S.M., Kelemen, P.B., Blusztajn, J., Clift, P.D., 2006. A detailed geochemical study of island arc crust: the Talkeetna arc section, south-central Alaska. J. Petrol. 47, 1051–1093.
Grove, T.L., Baker, M.B., 1984. Phase equilibrium controls on the tholeiitic versus calc-alkaline differentiation trends. J. Geophys. Res. 89, 3253–3274.
Haschke, M., Gunther, A., 2003. Balancing crustal thickening in arcs by tectonic vs. magmatic means. Geology 31, 933–936.
Hauri, E.H., Wagner, T.P., Grove, T.L., 1994. Experimental and natural partitioning of Th, U, Pb and other trace elements between garnet, clinopyroxene and basaltic melts. Chem. Geol. 117, 149–166.
Hildreth, W., Moorbath, S., 1988. Crustal contributions to arc magmatism in the Andes of central Chile. Contrib. Mineral. Petrol. 98, 455–489.
Hill, D.P., 1972. Crustal and upper mantle structure of the Columbia Plateau from long range seismic refraction measurements. Geol. Soc. Am. Bull. 83, 1639–1648.
Hirose, K., Kawamoto, T., 1995. Hydrous partial melting of lherzolite at 1 GPa: the effect of H_2O on the genesis of basaltic magmas. Earth Planet. Sci. Lett. 133, 463–473.
Hofmann, A.W., 1988. Chemical differentiation of the Earth: the relationship between mantle, continental crust, and oceanic crust. Earth Planet. Sci. Lett. 90, 297–314.
Humphreys, E.D., 1995. Post-Laramide removal of the Farallon slab, Western United States. Geology 23, 987–990.
Humphreys, E., Hessler, E., Dueker, K., Farmer, G., Erslev, E., Atwater, T., 2003. How Laramide-age hydration of North American lithosphere by the Farallon slab controlled subsequent activity in the Western United States. Int. Geol. Rev. 45, 575–595.
Ionov, D.A., 2010. Petrology of mantle wedge lithosphere: new data on supra-subduction zone peridotite xenoliths from the andesitic Avacha volcano, Kamchatka. J. Petrol. 51, 327–361.
Ionov, D., Chanefo, I., Bodinier, J.-L., 2005. Origin of Fe-rich lherzolites and wehrlites from Tok, SE Siberia by reactive melt percolation in refractory mantle peridotites. Contrib. Mineral. Petrol. 150, 335–353.
Jagoutz, O., Burg, J.P., Hussain, S., Dawood, H., Pettke, T., Iizuka, T., Maruyama, S., 2009. Construction of the granitoid crust of an island arc part I: geochronological and geochemical constraints from the plutonic Kohistan (NW Pakistan). Contrib. Mineral. Petrol. 158, 739–755.
Jagoutz, O., Müntener, O., Schmidt, M.W., Burg, J.P., 2011. The roles of flux-and decompression melting and their respective fractionation lines for continental crust formation: evidence from the Kohistan arc. Earth Planet. Sci. Lett. 303 (1), 25–36.
Johnson, K.T.M., Dick, H.J.B., Shimizu, N., 1990. Melting in the oceanic upper mantle: an ion microprobe study of diopsides in abyssal peridotites. J. Geophys. Res. 95, 2661–2678.
Kay, S.M., Coira, B., Viramonte, J., 1994. Young mafic back arc volcanic rocks as indicators of continental lithospheric delamination beneath the Argentine Puna plateau, central Andes. J. Geophys. Res. 99, 24323–24339.
Kepezhinskas, P., Defant, M.J., Drummond, M.S., 1996. Progressive enrichment of island arc mantle by melt-peridotite interaction inferred from Kamchatka xenoliths. Geochim. Cosmochim. Acta 60, 1217–1229.
Kessel, R., Ulmer, P., Pettke, T., Schmidt, M.W., Thompson, A.B., 2005. The water–basalt system at 4 to 6 GPa: phase relations and second critical endpoint in a K-free eclogite at 700 to 1400 °C. Earth Planet. Sci. Lett. 237, 873–892.
Kolodny, Y., Epstein, S., 1976. Stable isotope geochemistry of deep sea cherts. Geochim. Cosmochim. Acta 40 (10), 1195–1209.
Larter, R.D., Vanneste, L.E., Morris, P., Smythe, D.K., 2003. Structure and tectonic evolution of the South Sandwich arc. Geol. Soc. (Lond.) Spec. Publ. 219, 255–284.
Le Roux, V., Bodinier, J.L., Tommasi, A., Alard, O., Dautria, J.M., Vauchez, A., Riches, A.J.V., 2007. The Lherz spinel lherzolite: refertilized rather than pristine mantle. Earth Planet. Sci. Lett. 259, 599–612.
Lee, C.-T.A., 2005. Trace element evidence for hydrous metasomatism at the base of the North American lithosphere and possible association with Laramide low-angle subduction. J. Geol. 113, 673–685.
Lee, C.-T.A., 2014. Physics and chemistry of deep continental crust recycling. In: Treatise on Geochemistry, vol. 2, pp. 423–451.
Lee, C.-T.A., Cheng, X., Horodyskyj, U., 2006. The development and refinement of continental arcs by primary basaltic magmatism, garnet pyroxenite accumulation, basaltic recharge and delamination: insights from the Sierra Nevada. Contrib. Mineral. Petrol. 151, 222–242.
Lee, C.-T.A., Harbert, A., Leeman, W.P., 2007a. Extension of lattice strain theory to mineral/mineral rare-earth element partitioning: an approach for assessing disequilibrium and developing internally consistent partition coefficients between olivine, orthopyroxene, clinopyroxene and basaltic melt. Geochim. Cosmochim. Acta 71, 481–496.
Lee, C.-T.A., Morton, D.M., Kistler, R.W., Baird, A.K., 2007b. Petrology and tectonics of Phanerozoic continent formation: from island arcs to accretion and continental arc magmatism. Earth Planet. Sci. Lett. 263, 370–387.
Lee, C.-T.A., Lee, T.C., Wu, C.-T., 2013. Modeling the compositional evolution of recharging, evacuating, and fractionating (REFC) magma chambers: implications

for differentiation of arc magmas. Geochim. Cosmochim. Acta. http://dx.doi.org/10.1016/j.gca.2013.08.009..

Lee, C.-T., Rudnick, R.L., Brimhall Jr, G.H., 2001a. Deep lithospheric dynamics beneath the Sierra Nevada during the Mesozoic and Cenozoic as inferred from xenolith petrology. Geochem. Geophys. Geosyst. 2.

Lee, C.-T., Yin, Q., Rudnick, R.L., Jacobsen, S.B., 2001b. Preservation of ancient and fertile lithospheric mantle beneath the southwestern United States. Nature 411, 69–73.

Lee, C.-T., Yin, Q., Rudnick, R.L., Chesley, J.T., Jacobsen, S.B., 2000. Osmium isotopic evidence for Mesozoic removal of lithospheric mantle beneath the Sierra Nevada, California. Science 289, 1912–1916.

Leeman, W.P., 1983. The influence of crustal structure on compositions of subduction-related magmas. J. Volcanol. Geotherm. Res. 18, 561–588.

Levin, V., Park, J., Brandon, M., Lees, J., Peyton, V., Gordeev, E., Ozerov, A., 2002. Crust and upper mantle of Kamchatka from teleseismic receiver functions. Tectonophysics 358, 233–265.

Liang, Y., Elthon, D., 1990. Geochemistry and petrology of spinel lherzolite xenoliths from Xalapasco de La Joya, San Luis Potosi, Mexico: partial melting and mantle metasomatism. J. Geophys. Res., Solid Earth 95, 15859–15877.

Luffi, P., Saleeby, J.B., Lee, C.-T.A., Ducea, M.N., 2009. Lithospheric mantle duplex beneath the central Mojave Desert revealed by xenoliths from Dish Hill, California. J. Geophys. Res. 114, B03202.

Luhr, J.F., Aranda-Gomez, J.J., 1997. Mexican peridotite xenoliths and tectonic terranes: correlations among vent location, texture, temperature, pressure, and oxygen fugacity. J. Petrol. 38, 1075–1112.

Matsukage, K.N., Kubo, K., 2003. Chromian spinel during melting experiments of dry peridotite KLB-1 at 1.0-2.5 GPa. Am. Mineral. 88, 1271–1278.

Mattey, D., Lowry, D., Macpherson, C., 1994. Oxygen isotope composition of mantle peridotite. Earth Planet. Sci. Lett. 128, 231–241.

Maury, R.C., Defant, M.J., Joron, J.-L., 1992. Metasomatism of the sub-arc mantle inferred from trace elements in Philippine xenoliths. Nature 360, 661–663.

McDonough, W.F., Sun, S.-S., 1995. The composition of the Earth. Chem. Geol. 120, 223–253.

McInnes, B.I.A., Gregoire, M., Binns, R.A., Herzig, P.M., Hannington, M.D., 2001. Hydrous metasomatism of oceanic sub-arc mantle, Lihir, Papua New Guinea: petrology and geochemistry of fluid-metasomatised mantle wedge xenoliths. Earth Planet. Sci. Lett. 188, 169–183.

Moore, J.G., Dodge, F.C.W., 1980. Late Cenozoic volcanic rocks of the southern Sierra Nevada, California: I. Geology and petrology. Geol. Soc. Am. Bull. 91, 1995–2038.

Mukhopadhyay, B., 1989. Petrology and geochemistry of mafic and ultramafic xenoliths from the Sierra Nevada batholith, Part 1. Ph.D. dissertation. Univ. of Texas, Dallas, p. 215.

Mukhopadhyay, B., Manton, W.I., 1994. Upper-mantle fragments from beneath the Sierra Nevada batholith: partial fusion, fractional crystallization, and metasomatism in a subduction related ancient lithosphere. J. Petrol. 35, 1417–1450.

Müntener, O., Ulmer, P., 2006. Experimentally derived high-pressure cumulates from hydrous arc magmas and consequences for the seismic velocity structure of lower arc crust. Geophys. Res. Lett. 33, L21308.

Nixon, P.H., Rogers, N.W., Gibson, I.L., Grey, A., 1981. Depleted and fertile mantle xenoliths from southern African kimberlites. Annu. Rev. Earth Planet. Sci. 9, 285–309.

Parkinson, I.J., Arculus, R.J., Eggins, S.M., 2003. Peridotite xenoliths from Grenada, Lesser Antilles island arc. Contrib. Mineral. Petrol. 146, 241–262.

Parkinson, I.J., Pearce, J.A., 1998. Peridotites from the Izu–Bonin–Mariana forearc (ODP Leg 125): evidence for mantle melting and melt-mantle interaction in a supra-subduction zone setting. J. Petrol. 39, 1577–1618.

Pearce, J.A., Barker, P.F., Edwards, S.J., Parkinson, I.J., Leat, P.T., 2000. Geochemistry and tectonic significance of peridotites from the South Sandwich arc-basin system, South Atlantic. Contrib. Mineral. Petrol. 139, 36–53.

Perkins, G., Sharp, Z., Selverstone, J., 2006. Oxygen isotope evidence for subduction and rift-related mantle metasomatism beneath the Colorado Plateau–Rio Grande rift transition. Contrib. Mineral. Petrol. 151, 633–650.

Peslier, A.H., Francis, D., Ludden, J., 2002. The lithospheric mantle beneath continental margins: melting and melt-rock reaction in Canadian Cordillera xenoliths. J. Petrol. 43, 2013–2047.

Plank, T., Langmuir, C.H., 1988. An evaluation of the global variations in the major element chemistry of arc basalts. Earth Planet. Sci. Lett. 90, 349–370.

Rehfeldt, T., Foley, S.F., Jacob, D.E., Carlson, R.W., Lowry, D., 2008. Contrasting types of metasomatism in dunite, wehrlite and websterite xenoliths from Kimberley, South Africa. Geochim. Cosmochim. Acta 72, 5722–5756.

Rosenbaum, J.M., Kyser, T.K., Walker, D., 1994. High temperature oxygen isotope fractionation in the enstatite–olivine–$BaCO_3$ system. Geochim. Cosmochim. Acta 58, 2653–2660.

Saleeby, J., 2003. Segmentation of the Laramide slab-evidence from the southern Sierra Nevada region. Geol. Soc. Am. Bull. 115, 655–668.

Saleeby, J., Ducea, M., Clemens-Knott, D., 2003. Production and loss of high-density batholithic root, southern Sierra Nevada, California. Tectonics 22, 1064.

Savin, S.M., Epstein, S., 1970. The oxygen and hydrogen isotope geochemistry of ocean sediments and shales. Geochim. Cosmochim. Acta 34, 43–63.

Sharp, Z.D., 1990. A laser-based microanalytical method for the in situ determination of oxygen isotope ratios of silicates and oxides. Geochim. Cosmochim. Acta 54, 1353–1357.

Stern, T.W., Bateman, P.C., Morgan, B., Newell, M.F., Peck, D.L., 1981. Isotopic U–Pb ages of zircon from the granitoids of the central Sierra Nevada, California. USGS Professional Paper 1185, 19.

Stosch, H.-G.n., 1982. Rare earth element partitioning between minerals from anhydrous spinel peridotite xenoliths. Geochim. Cosmochim. Acta 46, 793–811.

Straub, S.M., Gomez-Tuena, A., Zellmer, G.F., Espinasa-Perena, R., Stuart, F.M., Cai, Y., Langmuir, C.H., Martin-Del Pozzo, A.L., Mesko, G.T., 2013. The processes of melt differentiation in arc volcanic rocks: insights from OIB-type arc magmas in the Central Mexican Volcanic Belt. J. Petrol. 54, 665–701.

Taira, A., 2001. Tectonic evolution of the Japanese island arc system. Annu. Rev. Earth Planet. Sci. 29, 109–134.

Takahashi, N., Suyehiro, K., Shinohara, M., 1998. Implications from the seismic crustal structure of the northern Izu–Bonin arc. Isl. Arc 7, 383–394.

Tatsumi, Y., 1986. Formation of the volcanic front in subduction zones. Geophys. Res. Lett. 13, 717–720.

Tatsumi, Y., Hamilton, D.L., Nesbitt, R.W., 1986. Chemical characteristics of fluid phase released from a subducted lithosphere and origin of arc magmas: evidence from high-pressure experiments and natural rocks. J. Volcanol. Geotherm. Res. 29 (1), 293–309.

Tatsumi, Y., Shukuno, H., Tani, K., Takahashi, N., Kodaira, S., Kogiso, T., 2008. Structure and growth of the Izu–Bonin–Mariana arc crust: 2. Role of crust-mantle transformation and the transparent Moho in arc crust evolution. J. Geophys. Res., Solid Earth 113 (B2), 1–19.

Taylor, S.R., 1977. Island arc models and the composition of the continental crust. In: Island Arcs, Deep Sea Trenches and Back-Arc Basins. AGU, Washington, DC, pp. 325–335.

Urrutia-Fucugauchi, J., Flores-Ruiz, J.H., 1996. Bouguer gravity anomalies and regional crustal structure in central Mexico. Int. Geol. Rev. 38, 176–194.

Valley, J.W., Kitchen, N., Kohn, M.J., Neindorf, C.R., Spicuzza, M.J., 1995. UWG-2, a garnet standard for oxygen isotope ratios: strategies for high precision and accuracy with laser heating. Geochim. Cosmochim. Acta 59, 5223–5231.

Van Kooten, G.K., 1980. Mineralogy, petrology, and geochemistry of an ultrapotassic basaltic suite, central Sierra Nevada, California, USA. J. Petrol. 21, 651–684.

Voigt, M., Handt, A., 2011. Influence of subsolidus processes on the chromium number in spinel in ultramafic rocks. Contrib. Mineral. Petrol. 162, 675–689.

Wallace, P.J., Carmichael, I.S.E., 1999. Quaternary volcanism near the Valley of Mexico: implications for subduction zone magmatism and the effects of crustal thickness variations on primitive magma compositions. Contrib. Mineral. Petrol. 135, 291–314.

Wernicke, B., Axen, G.J., Snow, J.K., 1988. Basin and Range extensional tectonics at the latitude of Las Vegas, Nevada. Geol. Soc. Am. Bull. 100, 1738–1757.

White, A.J.R., Chappell, B.W., 1977. Ultrametamorphism and granitoid genesis. Tectonophysics 43, 7–22.